International Journal of
*Molecular Sciences*

MDPI

*Article*

# Study on Doxorubicin Loading on Differently Functionalized Iron Oxide Nanoparticles: Implications for Controlled Drug-Delivery Application

**Vladislav R. Khabibullin [1,2], Margarita R. Chetyrkina [3], Sergei I. Obydennyy [4,5], Sergey V. Maksimov [1], Gennady V. Stepanov [2] and Sergei N. Shtykov [6,*]**

1 Chemistry Department, Lomonosov Moscow State University, Lenin Hills, 119991 Moscow, Russia
2 State Scientific Center of the Russian Federation, Joint Stock Company "State Order of the Red Banner of Labor Research Institute of Chemistry and Technology of Organoelement Compounds", 105118 Moscow, Russia
3 Skolkovo Institute of Science and Technology, 143026 Moscow, Russia
4 Dmitry Rogachev National Medical Research Center of Pediatric Hematology, Oncology and Immunology, 117198 Moscow, Russia
5 Center for Theoretical Problems of Physicochemical Pharmacology, 119334 Moscow, Russia
6 Department of Analytical Chemistry and Chemical Ecology, Institute of Chemistry, Saratov State University, 410012 Saratov, Russia
* Correspondence: shtykovsn@mail.ru

**Abstract:** Nanoplatforms applied for the loading of anticancer drugs is a cutting-edge approach for drug delivery to tumors and reduction of toxic effects on healthy cells. In this study, we describe the synthesis and compare the sorption properties of four types of potential doxorubicin-carriers, in which iron oxide nanoparticles (IONs) are functionalized with cationic (polyethylenimine, PEI), anionic (polystyrenesulfonate, PSS), and nonionic (dextran) polymers, as well as with porous carbon. The IONs are thoroughly characterized by X-ray diffraction, IR spectroscopy, high resolution TEM (HRTEM), SEM, magnetic susceptibility, and the zeta-potential measurements in the pH range of 3–10. The degree of doxorubicin loading at pH 7.4, as well as the degree of desorption at pH 5.0, distinctive to cancerous tumor environment, are measured. Particles modified with PEI were shown to exhibit the highest loading capacity, while the greatest release at pH 5 (up to 30%) occurs from the surface of magnetite decorated with PSS. Such a slow release of the drug would imply a prolonged tumor-inhibiting action on the affected tissue or organ. Assessment of the toxicity (using Neuro2A cell line) for PEI- and PSS-modified IONs showed no negative effect. In conclusion, the preliminary evaluation of the effects of IONs coated with PSS and PEI on the rate of blood clotting was carried out. The results obtained can be taken into account when developing new drug delivery platforms.

**Keywords:** doxorubicin; sorption; iron oxide nanoparticles; surface functionalization; magnetic properties; cell viability



**Citation:** Khabibullin, V.R.; Chetyrkina, M.R.; Obydennyy, S.I.; Maksimov, S.V.; Stepanov, G.V.; Shtykov, S.N. Study on Doxorubicin Loading on Differently Functionalized Iron Oxide Nanoparticles: Implications for Controlled Drug-Delivery Application. *Int. J. Mol. Sci.* **2023**, *24*, 4480. https://doi.org/10.3390/ijms24054480

Academic Editors: Lucia Ya. Zakharova and Ruslan R. Kashapov

Received: 23 January 2023
Revised: 19 February 2023
Accepted: 22 February 2023
Published: 24 February 2023



## 1. Introduction

Doxorubicin (DOX) and other antibiotics from the anthracycline series attract the attention of the scientific community due to the simultaneous combination of positive and negative effects on human body [1–4]. Furthermore, DOX plays a key role in the treatment of many neoplastic diseases, in particular cancer, even though its prolonged action causes cardiomyopathy and congestive heart failure [5,6]. A strong desire to reduce cardio- and nephrotoxicity of DOX led to the idea of binding the drug to various nanomaterials, e.g., engineered nanoparticles [7]. Various nano-sized structures based on synthetic and natural polymers, solid lipids and lipid nanoemulsions (liposomes), silver, gold, calcium carbonate, metal–organic frameworks, carbon, silicon, or magnetic materials have been

proposed as controlled delivery systems for doxorubicin [8–11]. Among nanocarbon materials, graphene, graphene oxide, carbon nanotubes, and fullerene are explored [12–17], with a focus on the toxicity and biocompatibility of the nanosystems in use. Nanoplatforms based on magnetic nanoparticles are the most commonly used for drug delivery, including DOX [18–22]. Their advantages include simplicity and cheap synthesis, biocompatibility, and the ability to efficiently adsorb the drugs that makes them ideal candidates for the reconstruction of a drug delivery platform. Despite the fact that the different ionic forms produced by iron oxide nanoparticles (IONs) after degradation can be easily assimilated by the body [23], there is still no unambiguous conclusion about the biocompatibility of IONs [24]. This stimulates further research in the field of biological applications of IONs [25–29]. An additional advantage of using IONs is their superparamagnetic properties, which make it feasible to control the drug delivery using an external magnetic field [8,30]. The IONs are also employed in magnetic resonance imaging, molecular imaging, hyperthermia, and cancer diagnostics [19,31–35]. Such attractive biomedical facets open an avenue for combining the specificity of drug delivery and magnetic resonance imaging, which enhances the effectiveness of anticancer therapy [36–38].

Due to the developed surface, the IONs tend to aggregate and oxidize. For this reason, their surface is coated with inorganic, organic, or polymeric materials that perform the functions of surface protection and selective functionalization, as reviewed by Zhu et al. [39]. It is important to note that the list of non-polymeric modifiers used for the loading and delivery of DOX is rather short, with a few contributions on IONs coated with silicon dioxide [40–42], gold [43], zinc oxide [44], and silicon dioxide activated with glutaric anhydride [45]. In addition, co-coating with carbon and/or gold conjugated with glutathione [46] and polypyrole [47] has been reported. Alternatively, magnetite can be covered with dimercaptosuccinic acid [48], citric acid [49], oleic acid [50], nonionic surfactants [50], and carbon [51].

In contrast, IONs are much more actively functionalized with synthetic and natural polymers for the purpose of DOX delivery [7,52–55]. Modification of the surface with polymers provides the sorbent with new useful properties, including pH and thermal sensitivity [56–59] and controlled drug release [60]. The polymer coating based on polyethylene glycol (PEG) helps reduce the drug degradation and thereby reduces the toxic effect on healthy cells [61]. Surface modification with the polysaccharides carrageenan [62], starch [63], cellulose [64], chitosan [65,66], and various conjugates based on polysaccharides [67–71] proved useful to enhance the selectivity of DOX release. The functionalization of IONs by proteins and large biomolecules also contributes to an increased efficiency of the use of IONs in cancer therapy [72,73]. Coating of IONs with heparin promotes anticoagulant activity and also has its own anticancer properties [74,75]. Described in recent literature is the use of nonionic polymers and block copolymers, as detailed in the Supplementary Materials Table S1. From the tabulated data, it is evident that the majority of alternative, ionic polymeric coatings contain the carboxyl group that renders a negative charge under sorption conditions and therefore electrostatic interactions with the protonated amino group of DOX. Among other valuable assets, most of the presented polymers are safe for in vivo use and are easily biodegradable.

Another promising direction in shaping cancer therapy is the use of magnetoliposomes [76,77]. Encapsulation of IONs into a liposome reduces the toxicity of the DOX and improves the IONs delivery, increases the DOX release, and also expands the possibilities for combining treatment methods [76,78–80]. However, there is a need to destroy the liposome prior to applying the combined chemotherapy with magnetic hyperthermia, which requires additional technical equipment [81].

It should be noted that sometimes the modifier adversely affects the biocompatibility of the material. The use of a cationic surfactant, CTAB, as a surface modifier increases the loading of DOX but reduces cell viability, causing the formation of pores in the cell membrane [82]. Therefore, the major aim of coating is to balance high sorption capacity, selectivity, and aggregative stability of nanoplatforms with their non-toxicity.

To reach the affected tissue, the IONs must pass through the capillaries and avoid phagocytosis, thus, their size should be less than 100 nm [83,84]. In addition, IONs must have a high magnetization which should disappear after the removal of the magnetic field in order not to cause the formation of aggregates [83,85]. Accordingly, the average size of IONs less than 100 nm or in the range of 100–150 nm is considered the best for loading and efficient drug delivery [7,86]. When choosing the proper size of IONs, it is also necessary to take into account the methods of their excretion from the body. It has been reported that particles up to 20 nm in diameter are removed from the blood through the kidneys, while particles > 100 nm, as a rule, are absorbed by the liver, spleen, or bone marrow [84].

A detailed analysis of available literature allows for several general conclusions. First, commonly used are the IONs of widely varied sizes, from small 6–10 nm, to medium (tens of nm), and quite large, over 100 nm and up to 300 nm. This is due to the fact that a priori it is unclear which particular size would provide the best targeting function [84,87,88]. For instance, for IONs ranging from 60 to 310 nm it was found that smaller nanoparticles demonstrate better cellular internalization, deeper penetration into multicellular spheroids, and provide higher efficiency of photothermal ablation in vitro. At the same time, large IONs are better accumulated in tumors, causing more effective inhibition of their growth. In their turn, 120 nm particles are best suited for magnetic resonance imaging and in vitro photoacoustic tomography. It is noted that apart from the size, the particle shape and the chemical composition of the modified surface may be important [89].

Second, in most studies the authors focus on block copolymers of complex structure (see Table S1). However, such techniques are of little use in the biomedical practice, since multi-stage synthesis is difficult and time-consuming. Furthermore, sorption and desorption processes on such modified particles sometimes last several days and have low efficiency. Third, only one type of ION surface modifier is usually subject to investigation. This shortcoming retards the choice of the most effective carrier for DOX. Likewise, little attention has been paid on the influence of the size and shape of the ION core.

The aim of this work was to (i) obtain IONs of 80–150 nm in size, (ii) modify their surface with cationic and anionic polyelectrolytes, nonionic polymer dextran, and porous carbon, and (iii) reveal the optimal core–shell system for the sorption of DOX, with the objective to develop and implement an effective nanocarrier for controlled drug delivery. The modified IONs were characterized in detail by various methods (XRD, FTIR, measuring the zeta-potential, scanning and transmission microscopy, etc.) to explain the sorption behavior.

## 2. Results and Discussion

### *2.1. Characterization of IONs*

#### 2.1.1. X-ray Diffraction

The crystal structures of $Fe_3O_4$ were characterized by X-ray diffractometer, as shown in Figure S1. Diffraction peaks at 2θ values around 30.11° (200), 35.61° (311), 43.13° (400), 53.67° (422), 57.17° (511), 62.77° (440), and 73.25° (533) correspond to the lattice planes of the face-centered cubic $Fe_3O_4$ phase [90,91], being in good agreement with the standard XRD data card of $Fe_3O_4$ crystals (JCPDS No.85–1436). The synthesis product, in addition to magnetite, contains fractions of hematite $Fe_2O_3$ and goethite FeO(OH), at 24 and 6%, respectively. High-temperature treatment (boiling) in propylene glycol reduced the proportion of hematite to 11%, while the goethite phase disappeared completely.

#### 2.1.2. SEM and TEM

The results of TEM and SEM measurements of particle size are presented here and in the Supplementary Materials Figures S2 and S3. The synthesized materials are a polydisperse ensemble of crystalline particles of cubic magnetite. Particle size ($d$) for unmodified magnetite $Fe_3O_4$, determined from TEM and SEM images, is in the range of 80–150 nm. The calculated values of $d$ were limited to a sample of 500 particles. The presence of fine ($d$ < 80) and larger ($d$ > 150) fractions does not exceed 10% by volume. Thus, the average particle

size ($d_{av}$) is 115 ± 35 nm. The TEM micrographs also show variable in size aggregates with a size of 300–400 nm.

Using HRTEM, the size of the magnetite particles after surface modification (PSS, PEI, and Carb) was determined to estimate the change in the size of the shell thickness after the sorption of DOX (see Section 3.6 for more detail). Based on TEM images, it was found that the shell for PSS- and PEI-modified IONs is uniform (Figure 1c,e). The thickness of MNPs is 11.6 ± 0.6 and 11.2 ± 2.6 nm for $Fe_3O_4$@PSS and $Fe_3O_4$@PEI, respectively. The thickness of the porous carbon layer in $Fe_3O_4$@Carb (Figure 1g,h) is substantially wider, 26.0 ± 6.7 nm. The TEM micrographs witness that the IONs coated with PSS and PEI are in an aggregated state while forming the chain structures (Figure S3). The reason may be the interaction between the polymer shells of MNPs as well as intrinsic limitations of TEM and SEM, operating in a high vacuum where particles tend to stick together.

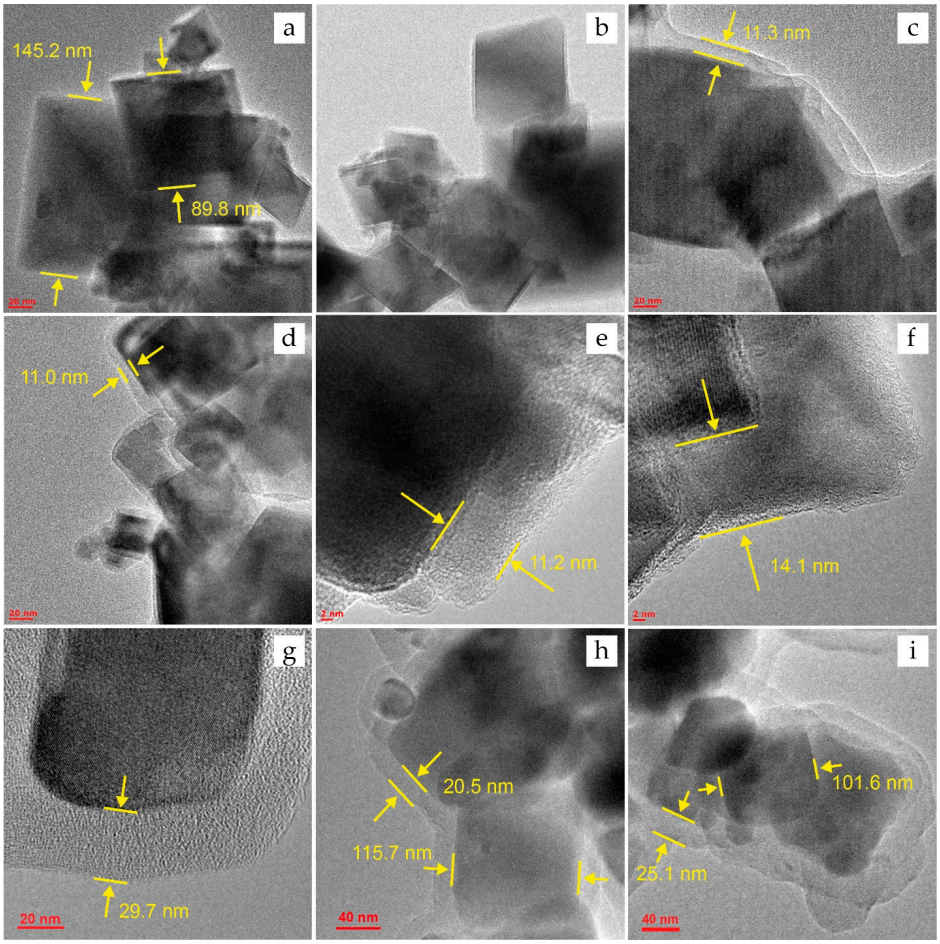


**Figure 1.** HRTEM images for the IONs before DOX sorption: (**a**)—$Fe_3O_4$, (**c**)—$Fe_3O_4$@PSS, (**e**)—$Fe_3O_4$@PEI, and (**g**,**h**)—$Fe_3O_4$@Carb; and after sorption of DOX: (**b**)—$Fe_3O_4$@DOX, (**d**)—$Fe_3O_4$@PSS@DOX, (**f**)—$Fe_3O_4$@PEI@DOX, and (**i**)—$Fe_3O_4$@Carb@DOX.

For unmodified magnetite, the particle sizes before (Figure 1a) and after DOX sorption (Figure 1b) are comparable. The presence of the drug was not detected on HRTEM-photographs, and the change in particle size is not significant, amounting less than 5% of the average size. The results for the modified materials also indicate the absence of noticeable changes in the particle morphology after the sorption of DOX: the shell thickness of $Fe_3O_4$@PSS@DOX was 11.0 ± 0.7 nm (Figure 1d), and for $Fe_3O_4$@Carb@DOX 26.1 ± 7.5 nm (Figure 1i). Changes for $Fe_3O_4$@PEI are more noticeable. After the sorption of the drug, the average shell thickness increased by 2.9 nm (the thickness of the $Fe_3O_4$@PEI@DOX shell was 14.1 ± 1.9, see Figure 1f), likely indicating the presence of DOX on the surface.

2.1.3. Infrared Spectroscopy

The IR spectra of the original magnetite and magnetite coated with porous carbon and polymers are shown in Figure 2. The summary of peak assignment, given in Table 1, confirms the successful surface modification.

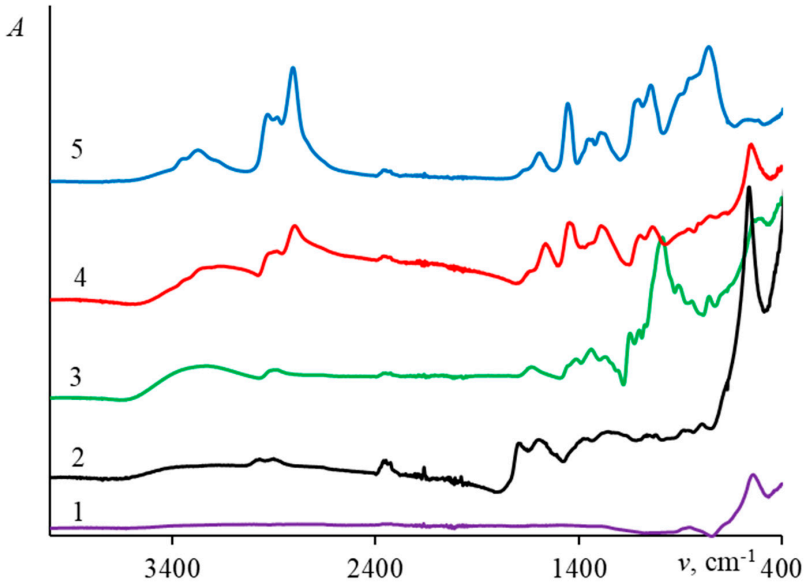


**Figure 2.** IR spectra of IONs covered by different surface modifiers: (1)—$Fe_3O_4$, (2)—$Fe_3O_4$@Carb, (3)—$Fe_3O_4$@Dex, (4)—$Fe_3O_4$@PEI, and (5)—$Fe_3O_4$@PSS.

**Table 1.** IR band assignment for modified magnetite particles.

| Surface Modifier | Wavenumber ($cm^{-1}$) | Assignment |
|---|---|---|
| pure $Fe_3O_4$ | 575 | Stretching vibrations of Fe–O bond [92] |
| PEI | 3200–3400 | Stretching vibrations of N–H bond [93] |
| | 2920 | Stretching vibrations of C–H groups of CH in PEI [94] |
| | 2780 | Stretching vibrations of C–H groups of $CH_2$ in PEI [91] |
| | 1560 | Deformation vibrations of C–N bond |
| | 1460 | Deformation vibrations of $CH_2$ group [95] |
| | 1037,1090 | Stretching vibrations of C–N bond [95,96] |
| Carb | 3300–3450 | Stretching vibrations of O–H bond |
| | 2950, 2880 | Stretching vibrations of C–H groups of CH in carbon [97] |
| | 1700, 1580 | Stretching vibrations of C=O bond [92,98] |
| | 1604 | Stretching vibrations of C=C bond [99] |
| | 1000–1450 | Stretching vibrations of C–O bond [98] |
| | 875–750 | Out-of-plane bending vibrations of aromatic CH groups [98] |
| Dex | 3200 | Stretching vibrations of O–H bond [100] |
| | 2900 | Stretching vibrations of C–H bond in -$CH_2$ group [100] |
| | 1636 | Stretching vibrations of C=O [101] |
| | 1344 | Stretching vibrations of C–O [100] |
| | 1105, 1075, and 1020–995, | Stretching vibrations of C–O–C ester group of dextran [100,102,103] |
| PSS | 2930, 2800 | Stretching vibrations of C–H bond in –$CH_3$ and –$CH_2$– groups [104] |
| | 1590 | Stretching vibration of a C–C bond in an aromatic ring |
| | 1350 | Vibrations of the O–S–O double bond in –$SO_3H$ group |
| | 1200 | Stretching vibrations of the O=S=O in –$SO_3H$ groups [105] |
| | 1110 | C–H bending vibrations of the aromatic ring |
| | 1120, 1152, and 1034 | S=O stretching vibrations of the sulfonic group [104,106] |
| | 770 | Bending vibrations of C–H |

The IR spectra of DOX itself and magnetite nanoparticles with adsorbed DOX are presented in Figure 3. In all cases the drug's spectrum is subject to drastic changes, indicating that its sorption does take place. The strongest spectral changes are observed upon sorption on the pure magnetite nanoparticles and $Fe_3O_4$ coated with porous carbon. Characteristic absorption peaks and their assignments are summarized in Table 2.

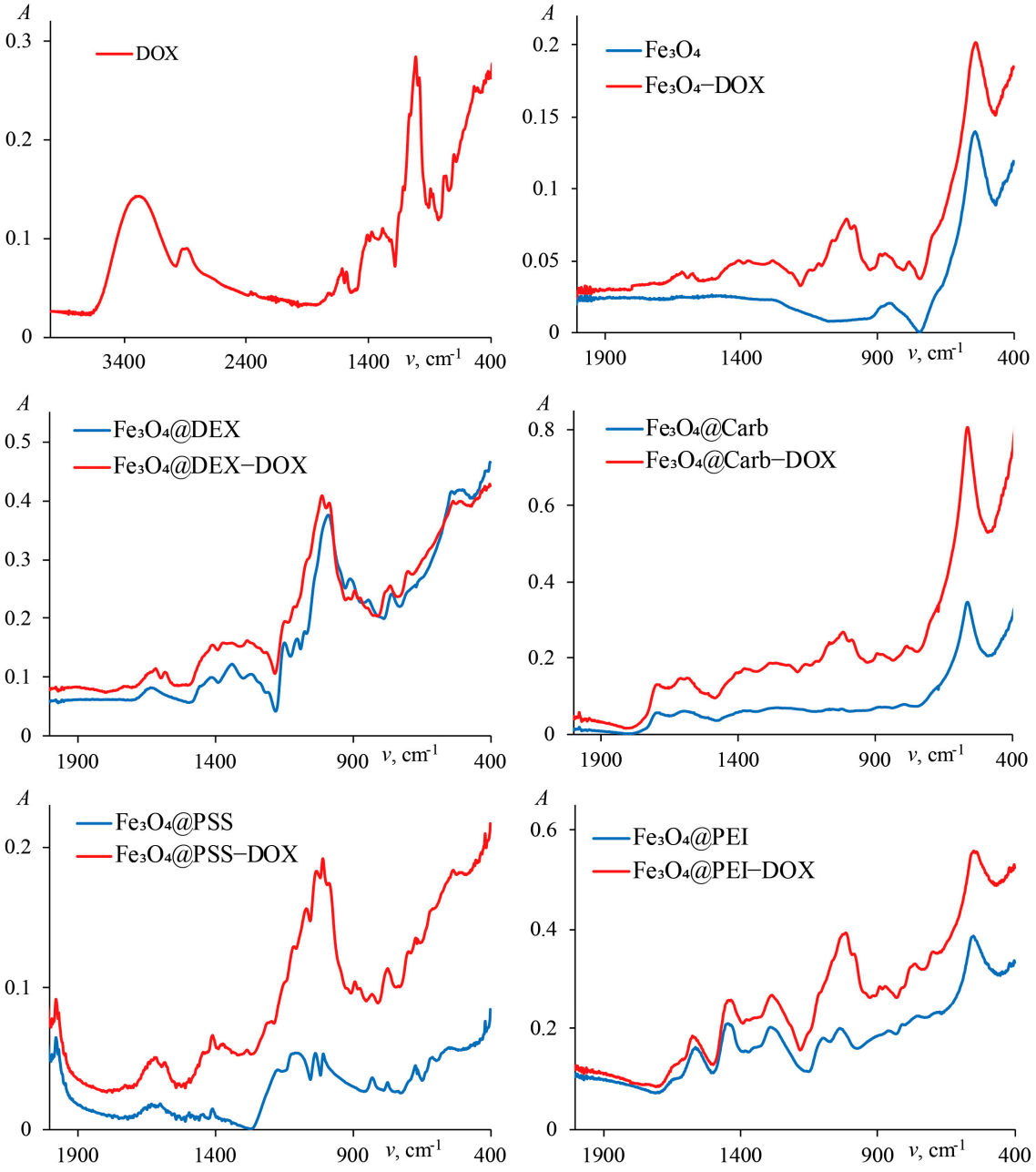


**Figure 3.** IR spectra of IONs covered by different surface modifiers with doxorubicin.

**Table 2.** Characteristic IR bands of doxorubicin and its conjugates with magnetite nanoparticles.

| Wavenumber ($cm^{-1}$) | Assignment |
|---|---|
| 3282 | Stretching vibrations of O–H bond |
| 2925, 2885 | Stretching vibrations of C–H bond in $–CH_2$ group [107] |
| 1725 | Stretching vibrations of C=O [107] |
| 1611, 1577, 1412 | C=C stretching vibrations of the aromatic ring [107] |
| 1105, 1067 | Stretching vibrations of C–O–C ester group [107] |
| 1008 | Deformation vibrations of C=O [108] |
| 693 | Stretching vibrations C=C ring bend [107] |

The change in the IR spectra after the sorption of DOX indicates the presence of the drug on the surface of the sorbents.

#### 2.1.4. Magnetic Characterization

The magnetic properties were measured using vibrating-sample magnetometry that assumes that the saturation magnetization (*Ms*) is related to the sample mass [109]. By a slightest change in the *Ms* and coercive force (*Hc*), it is possible to detect not only changes in the internal structure of the magnetic material and pertinent chemical processes (particle growth, oxidation, etc.), but also changes in the mass of the sample with high accuracy [70,110].

As can be seen from Figure S4 and Table 3, implementation of the modifiers slightly reduces the magnetization compared to the parent magnetite. Specifically, functionalization with polymers, regardless of their nature, results in a magnetization decrease of almost 10%. This may indicate small differences in the thickness of the modifier layer on the magnetite surface, shielding the magnetic core and hence reducing its magnetic moment [69]. For $Fe_3O_4$@Carb, the magnetization is reduced by 20%. Importantly, for all types of nanoparticles under scrutiny, superparamagnetic behavior is observed with a characteristic absence of residual magnetization and an insignificant $H_C$ of 5.0 mT. This phenomenon presents a crucial factor for using magnetic drug carriers in the biomedical field. As already mentioned above, one of IONs' positive features is that after the removal of the external magnetic field, there is no residual magnetization, which causes the aggregation of magnetic particles. After the sorption of DOX, a slight change in the saturation magnetization was observed (Table 3) and additionally to IR-spectra and HRTEM images, this finding indicates the presence of the drug on the adsorbent and an increase in the thickness of the nonmagnetic layer of the particle. The change in *Ms* was no more than 4%. The greatest change is observed in PEI- and carbon-modified IONs.

**Table 3.** Magnetic properties of IONs coated with various modifiers before and after sorption of DOX.

| Sample | *Ms* ($emu \cdot g^{-1}$) | | Δ (%) |
|---|---|---|---|
| | Before | After | |
| $Fe_3O_4$ | 77.7 | 77.6 | <1 |
| $Fe_3O_4$@PSS | 71.1 | 69.3 | 3 |
| $Fe_3O_4$@PEI | 70.5 | 67.8 | 4 |
| $Fe_3O_4$@Dex | 70.2 | 70.0 | <1 |
| $Fe_3O_4$@Carb | 60.8 | 58.4 | 4 |

#### 2.1.5. Zeta-Potential Measurements

Results of determining the zeta-potential of functionalized IONs are presented in Figure 4. In all cases, surface modification significantly changes the $\zeta$ of the initial magnetite. For the polyelectrolyte-modified particles, the $\zeta$ exceeds the accepted stability threshold ($\zeta > |30|$ mV [111]) at most of the examined pH values so that one could expect their improved stability behavior in suspensions. Nanoparticles coated with porous carbon have a negative $\zeta$ over the entire pH range, but only at pH $\geq$ 10 does its value (−34 mV)

correspond to the mentioned stability condition. The most plausible reason of this observation is the presence (and dissociation in an alkaline medium) of carboxyl and hydroxyl groups on the surface of porous carbon. Coating with dextran reduces the surface charge by virtue of the particle enveloping with a polymer shell, built-up via the mechanism of hydrogen bond formation [112]. At the same time, in the region of pH 5.5, an isoelectric point was observed.

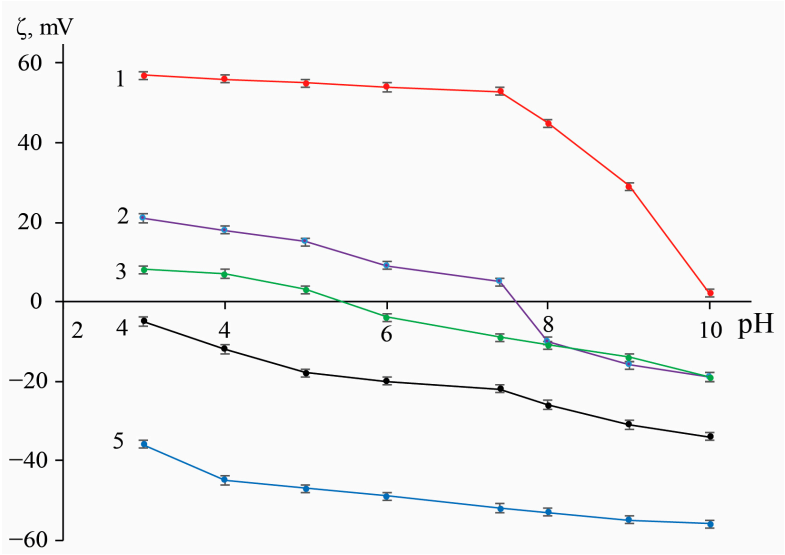


**Figure 4.** pH-responsive zeta-potential of original and functionalized IONs. Traces: (1)—$Fe_3O_4$@PSS, (2)—$Fe_3O_4$@Carb, (3)—$Fe_3O_4$@Dex, (4)—$Fe_3O_4$, and (5)—$Fe_3O_4$@PEI ($n$ = 3, $p$ = 0.95).

### 2.2. Assessment of Colloidal Stability

An important characteristic for dispersion of nanoparticles is stability over time. The stability of magnetite suspensions might be low because of rather large particle sizes. Here, to assess the sedimentation stability, the method of sedimentation in a gravitational field presented in the Supplementary Materials (Procedures) was used [113]. To evaluate the effect of modification chemistry on colloidal stability, the time during which the particle sedimentation takes place was measured (Figure S5). The data obtained, as well as the results of measuring the hydrodynamic diameter $d_{av}$ (Z-average size) of samples, are collected in Table 4.

**Table 4.** Colloidal stability, zeta-potential, and hydrodynamic size of aqueous suspensions with concentration 50 mg·mL$^{-1}$ at 25 °C ($n$ = 3, $p$ = 0.95).

| Sample | Average Settling Time (min) | | ζ-Potential (mV) | | Z-Average Size (nm) [a] | |
|---|---|---|---|---|---|---|
| | pH 5.0 | pH 7.4 | pH 5.0 | pH 7.4 | pH 5.0 | pH 7.4 |
| $Fe_3O_4$ | 2.3 ± 0.1 | 2.0 ± 0.1 (2.1) [b] | 15 ± 1 | 5 ± 1 | 126 ± 4 | 151 ± 3 |
| $Fe_3O_4$@PEI | 8.5 ± 0.2 | 8.5 ± 0.2 (8.3) | 55 ± 1 | 53 ± 1 | 95 ± 2 | 97 ± 2 |
| $Fe_3O_4$@PSS | 3.4 ± 0.1 | 10.3 ± 0.1 (10.1) | −47 ± 1 | −52 ± 1 | 118 ± 5 | 118 ± 7 |
| $Fe_3O_4$@Dex | <1 | 7.8 ± 0.2 (7.8) | 3 ± 1 | −9 ± 1 | 282 ± 9 | 130 ± 2 |
| $Fe_3O_4$@Carb | ~1 | ~1 (~1) | −18 ± 1 | −22 ± 1 | 296 ± 8 | 290 ± 9 |

[a] Measured immediately after evaluation of colloidal stability. [b] Given in parentheses is the average sedimentation time after the sorption of DOX.

The DLS measurements give only an approximate size of the MNPs because they are very sensitive to temperature, solvent viscosity, and the presence of "shell" around particles [114]. For TEM, the dried samples are to be used, since the method works under ultra-high vacuum conditions. For this reason, the average particle size obtained by DLS is usually higher [114]. Diagrams of the distribution of particle size by intensity are presented in Figure S6.

The data of Table 4 show that in all cases the stability of MNPs is not high and it is limited to 11 min. On the other hand, the tested nanomaterials demonstrate a different sedimentation rate, which indicates the important role of the surface modifier. The sedimentation time, zeta-potential, and hydrodynamic size of $Fe_3O_4$@PEI remain practically unchanged at both pH values and their sedimentation proceeds quite slowly due to the high $\zeta$. The $Fe_3O_4$@PSS particles have the best stability in suspension at pH 7.4 due to the complete dissociation of modifier's sulfonic groups. Unusual increased stability in the colloidal solution of IONs coated with dextran at pH 7.4, despite the lowest $\zeta$ values, can be explained by the steric factor [115]. On the other hand, the $Fe_3O_4$@Carb suspension displays marginal stability (see Table 4), as an effect of large particle size and low zeta-potential. Changes in the rate of colloidal stability after sorption of DOX were not observed. The value of the sedimentation rate of IONs loaded with DOX did not change significantly and was within experimental error (see Table 4, values in parentheses).

Thus, based on the results of Sections 2.1.3 and 2.1.5 on the study of the sorption of various modifiers on the surface of MNPs, as well as the literature data on the state of bare magnetite nanoparticles and polymers in an aqueous solution at pH 7.4, we can assume that this sorption is caused by the complex various types of interactions. Since, at this pH, the amino groups of PEI are partially protonated, and the OH groups on the magnetite surface are partially dissociated, its binding to the polyelectrolyte is due to both electrostatic interaction and the participation of the H-bond [91,116]. In the case of PSS, the negatively charged sulfonic groups of the polymer interact electrostatically with surface iron cations and simultaneously form H-bonds with the surface OH groups of the magnetite. The binding of dextran and porous carbon to magnetite is also caused by electrostatic forces, van der Waals interactions, and H-bonding [99–102,117].

### 2.3. Sorption of Doxorubicin

Figure 5 shows typical sorption isotherms and dependences of the degree of sorption on the mass of the sorbent. The highest degree of sorption (65%) is achieved when using the $Fe_3O_4$@PEI nanoparticles, the outcome being in accord with their highest zeta-potential (+53 mV). It can be assumed that under these conditions, sorption takes place through the formation of hydrogen bonds between non-protonated amino groups of PEI and heteroatoms of the phenolic, alcohol, methoxy, and amino groups of DOX. According to Suh et al. [118], at pH 7.4 about 80% of amino groups of PEI, which can participate in the formation of H-bonds with DOX, are not protonated. In turn, at this pH about half of the DOX amino groups are also not protonated [119–121]. Our assumption is consistent with the findings of a study by Coluccini et al. [122], who by applying the $^1$H NMR spectroscopy as well as NOESY and NOE NMR analysis in $D_2O$ found out that the chemical shifts of the protons of the proton-donor groups and aromatic rings of DOX, PEI are all subject to alterations upon the addition of PEI.

A higher degree of drug loading onto $Fe_3O_4$@Carb (compared to unmodified IONs or $Fe_3O_4$@Dex) is presumably associated with the shell porous structure. Increased negative potential favors the electrostatic interaction of IONs with the drug cation formed due to the partial protonation of the DOX amino group [121]. Such interpretation is consistent with an even a higher degree of sorption (32%) by $Fe_3O_4$@PSS particles, whose negative zeta-potential at pH 7.4 is higher than that at pH 5.0. An additional factor for increasing the degree of sorption by $Fe_3O_4$@PSS may be the hydrophobic interaction of modifier's benzene rings with the hydrophobic parts of the drug molecule. From the data of Figure 5b, it follows that a 95% sorption of DOX (0.5 mg) into nanoparticulate form requires from 2 mg $Fe_3O_4$@PEI and 15 mg $Fe_3O_4$@PSS to 25 mg $Fe_3O_4$@Carb and more than 30 mg $Fe_3O_4$@Dex (all sorbents being considerably more efficient than $Fe_3O_4$).

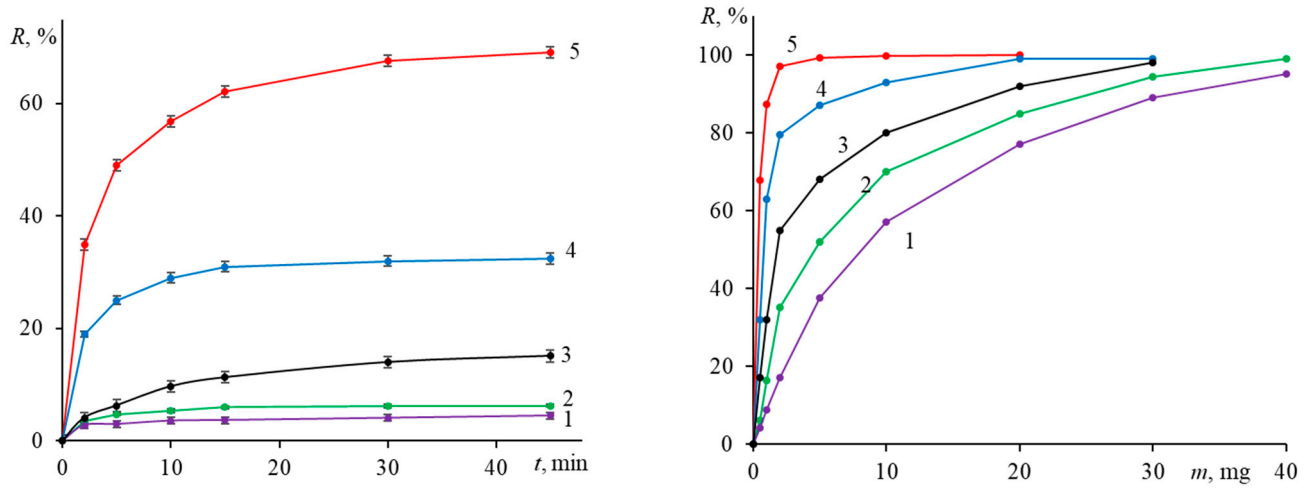


(**a**) (**b**)

**Figure 5.** Time- and sorbent mass-dependent sorption of doxorubicin on various IONs. Conditions: (**a**) $m_0$ = $m_S$ = 0.5 mg and (**b**) $m_S$ = 0.5 mg; time 45 min, pH 7.4, 25 °C. Traces: (1)—$Fe_3O_4$, (2)—$Fe_3O_4$@Dex, (3)—$Fe_3O_4$@Carb, (4)—$Fe_3O_4$@PSS, and (5)—$Fe_3O_4$@PEI. ($n$ = 3, $p$ = 0.95).

To gain a deeper understanding of the characteristics of the synthesized sorbents, we compared them with other reported nanosized sorbents used for loading DOX (see Table S2). The PEI- and PSS-functionalized IONs of interest have a higher sorption capacity (691 and 325 mg·g$^{-1}$, respectively). Such a difference can be explained by the fact that in the case of PEI, the interaction with DOX involves all oxygen-containing groups of DOX and amino groups of PEI, whereas PSS can interact electrostatically only with the protonated amino group of DOX. This explains the larger amount of the PSS-sorbent required for the sorption of DOX.

Another benefit of the modified IONs is much shorter time required for making quantitative drug loading true. However, the most principal advantage comprises the potential of magnetic site-specific targeting, when the drug is delivered to the deceased tissue or organ by means of external magnetic field.

### *2.4. Adsorption Kinetics*

Comparison of the efficiency of DOX sorption on all sorbents of our interest follows from Figure 6, with all the fitting kinetic parameters listed in Table 5. The initial adsorption stage is rapid as the DOX molecules incline to be bound onto an external, highly developed surface of the nanoparticles. The correlation coefficients ($R^2$) presented in Table 5 witness that the pseudo-second-order kinetic model describes the process of DOX adsorption more precisely. This confirms that adsorption depends on the amount of the drug and the active sites on the surface of the sorbent. It is interesting to note that the calculated values of $q_e$, determined by the pseudo-second-order model, are larger than the experimental ones (Table 5). This may indicate the need for employing longer sorption times.

Thus, immobilization of DOX on nanoparticles may take place due to the electrostatic and van der Waals interactions, hydrogen bonds, and π–π stacking of the anthracycline DOX fragment with aromatic fragments of the coating material [122]. Thus, it is difficult to predict what factor(s) governs the efficiency and degree of immobilization.

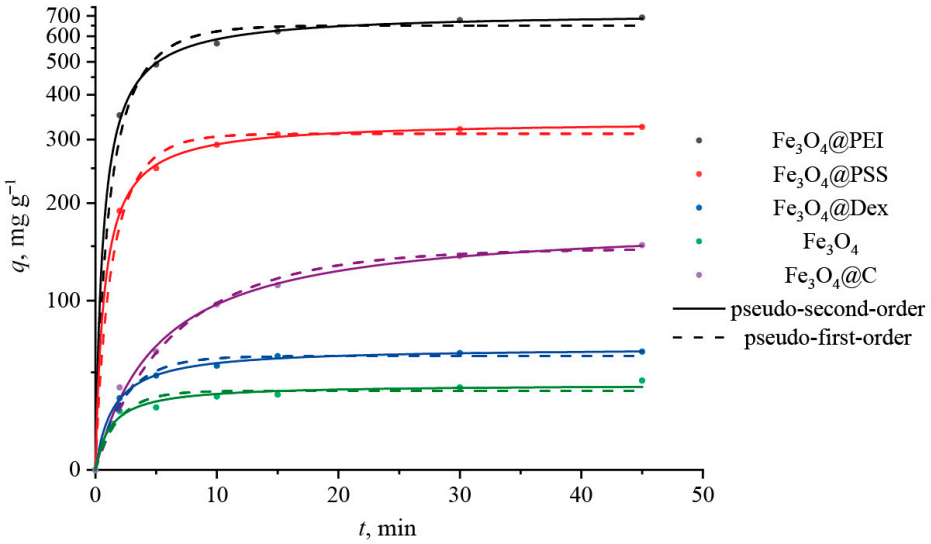


**Figure 6.** Adsorption kinetic curves of DOX onto different magnetite nanoparticles.

**Table 5.** Kinetic parameters of the pseudo-first- and pseudo-second-order for the sorption of DOX at 25 °C.

| Sample | $q_e^{exp}$ (mg g$^{-1}$) | Pseudo-First Order | | | Pseudo-Second Order | | |
|---|---|---|---|---|---|---|---|
| | | $q_e$ (mg g$^{-1}$) | $k_1$ | $R^2$ | $q_e$ (mg g$^{-1}$) | $k_2$ | $R^2$ |
| $Fe_3O_4$/PEI | 690 ± 10 | 649 ± 22 | 0.31 ± 0.05 | 0.972 | 719 ± 9 | 6.10 ± 0.04 | 0.998 |
| $Fe_3O_4$/PSS | 325 ± 10 | 311 ± 8 | 0.40 ± 0.05 | 0.982 | 337 ± 9 | 18.00 ± 0.01 | 0.999 |
| $Fe_3O_4$/Carb | 151 ± 8 | 147 ± 5 | 0.11 ± 0.01 | 0.986 | 178 ± 5 | 6.70 ± 0.08 | 0.996 |
| $Fe_3O_4$/Dex | 63 ± 7 | 60 ± 2 | 0.37 ± 0.05 | 0.979 | 66 ± 1 | 84.00 ± 0.06 | 0.998 |
| $Fe_3O_4$ | 39 ± 8 | 39 ± 2 | 0.49 ± 0.15 | 0.913 | 42 ± 2 | 0.016 ± 0.005 | 0.965 |

### *2.5. Desorption of DOX*

An important step in developing the ION-based drug delivery system was the verification of drug release. To study the applicability of modified IONs as carriers of anticancer drugs, the behavior of DOX release was modeled at physiological (pH 7.4) and cancer cell pH (pH 5.0) The resulting kinetic profiles are depicted in Figures 7 and S7, the latter portrays the first 60 min of desorption.

As noted in many studies, desorption of DOX at pH 7.4 proceeds 2–4 times slower than in a slightly acidic environment [10,123–125]. The same behavior was observed in our experiments. As shown in Figure 7a, all samples showed no significant drug release (<7%) at pH 7.4. This collective behavior of sorbents is associated with a strong electrostatic interaction between sorbent and sorbate. Additionally, this may be due to the poor solubility of the drug itself with an increasing the pH [126]. At the same time, abrupt initial desorption (Figure S7), which is observed in all samples during the first 15–30 min, is associated with the weak physical adsorption of some drug molecules on the surface of MNPs.

On the other hand, as the pH decreases, as shown in Figure 7b, drug desorption increases. In all cases, at pH 5.0, the drug is only partially desorbed, with a highest release of about 30% recorded for the PSS-modified IONs. It is important to mention that within the first 30 min, i.e., the timeframe simulating in vivo application of a magnetic nanoformulation, DOX release reaches up to 15%. This would generate drug active concentration of 0.14 mmol·L$^{-1}$ and 2–3 times higher that could be achieved with other nanosorbents [127–129].

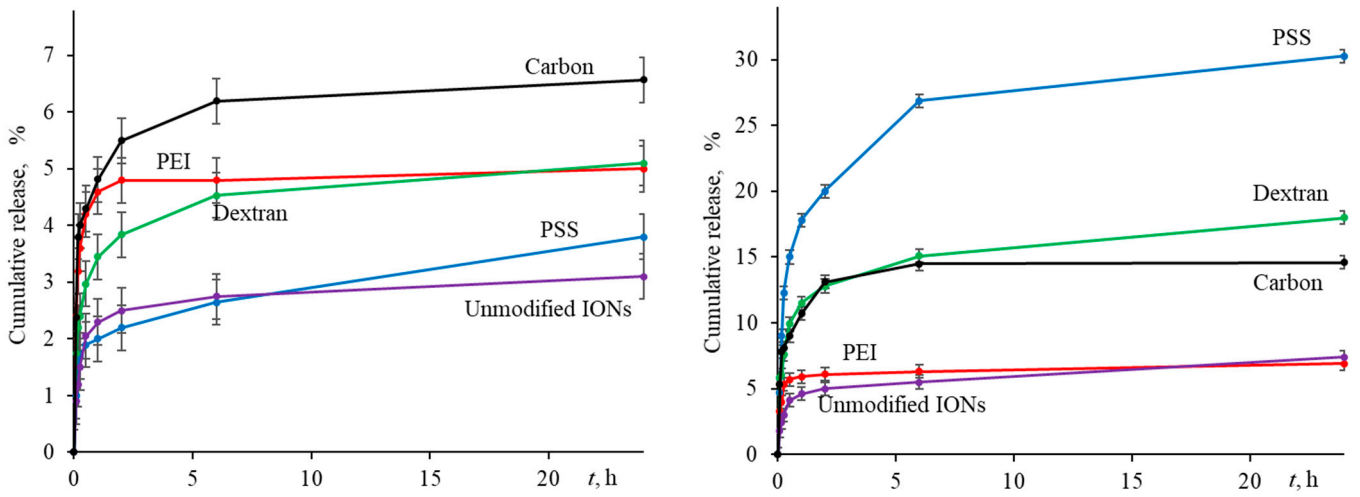


**Figure 7.** Payload release from drug-loaded nanosorbents in buffer solution at (**a**) pH 7.4 and (**b**) pH 5.0 as a function of time ($n$ = 3, $p$ = 0.95).

The IONs coated with Dex and Carb demonstrate relatively easy desorption in an acidic environment (but not to the full extent). In the case of Dex, two phenomena can play a role here. On the one hand, the zeta-potential (in absolute units) decreases with decreasing the pH and passes through the isobestic point at the region of pH 5.5, hence implying a weakening of electrostatic interactions and increasing the release of the drug. Similar results were observed by Liu et al. [69] for the DOX desorption from the surface of modified carboxymethylchitosan. On the other hand, a decrease in pH reduces the solubility of Dex-modified IONs (see Section 2.2) and increases their aggregation [115], which can hinder the drug release over time.

In the case of the Carb coating, we assume the presence of two types of localization of the drug on the surface. In the first case, DOX is attached to the surface due to electrostatic forces, and a change in the zeta-potential led to a decrease in forces and desorption of the drug. In the second case, the drug enters the cavities of porous carbon layer, making desorption extremely difficult to achieve. It is possible that additional conditions are required for such desorption mechanism such as the magnetic-field-induced drug release [130].

In our opinion, a slow (but sufficient) release of the drug can be considered as a positive factor, ensuring its long and uniform cell-killing action. In therapeutic practice, this would allow for preventing repeated exposure, drug overdosage, and possibly reducing its negative side effects. From this viewpoint, the $Fe_3O_4$@PEI nanoparticles may have the greatest medicinal potential, with low release efficiency compensated by high sorption capacity.

### *2.6. Cell Viability Analysis*

The cytotoxicity of DOX and IONs is well known. Therefore, our relevant interest was directed to the modifiers PSS and PEI. Whereas PSS in the free form is well studied, for instance in the treatment of hyperkalemia [131], where it showed no measurable cytotoxicity [132,133], PEI proved to be a highly toxic agent capable of initiating apoptosis and cell necrosis [134–136]. Moreover, as noted by Kafil et al., branched PEI is more harmful than a linear analog [134]. Furthermore, it was shown that an increase in the molecular weight of PEI inhibits the cell proliferation [137].

The widely used MTT assay has a number of limitations and is only capable of assessing cytotoxicity based on the metabolic activity of the cell according to the "living–non-living" principle [138]. At the same time, the mechanism by which this or that agent

affects the cells remains beyond the scope of the analysis. It is also impossible to transfer the properties of individual components to the entire system, which forced us to consider modifiers not as separate substances, but in combination with the core entity. The results acquired revealed that the presence of the $Fe_3O_4$@PEI and $Fe_3O_4$@PSS NPs in the cell medium (for both materials) did not statistically reduce cell survival. Figure 8 shows the percentage of living cell depending on the concentration of particles added to the cell medium. It is clear that all of the tested particles and concentrations did not affect cells viability remaining no less than 75–80%.

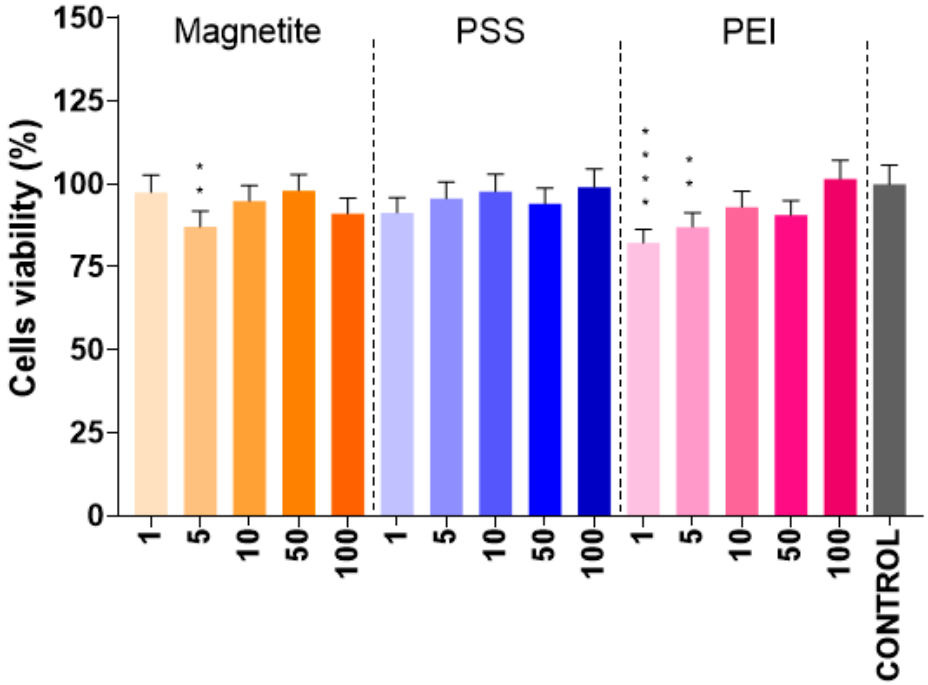


**Figure 8.** Results of the cell viability MTT test for N2A cells incubated with parent and modified IONs. The abscissa numbers represent concentration of nanoparticles (in $\mu g \cdot L^{-1}$); the *p* values (<0.01 and <0.0001) are marked, respectively, with, two, and four asterisks.

The most intriguing result is the impact of small doses of IONs (5 $\mu g \cdot L^{-1}$) and PEI-modified IONs (5 and 1 $\mu g \cdot L^{-1}$), as statistical analysis by non-parametric one-way ANOVA indicated their difference with the control group. Probably, this could be related to the better availability of particles for cells at small concentrations compared to applying higher concentrations, at which the particles can agglomerate and become unavailable to cells.

### *2.7. Real-Time Platelet Dynamics*

Biocompatibility testing involves a systematic approach with many different assays. As a preliminary trial, we studied the effect of IONs on the rate of thrombus formation. $Fe_3O_4$ nanoparticles, as previously found, have high biocompatibility with blood and are widely used in vitro and in vivo assays [25,139]. The presence of magnetite nanoparticles does not cause degradation of blood cells (leukocytes, thrombocytes, and erythrocytes) or noticeable side effects [140]. However, in our case, MNPs have a developed surface, imposing various interactions with blood cells. The rate of thrombus formation on the surface of glass coated with collagen was assessed during the first 10 min for three different MNPs: $Fe_3O_4$@PSS, $Fe_3O_4$@PEI, and $Fe_3O_4$. Blood without the addition of nanoparticles was used as a control.

For the control sample, the rate of thrombus formation, as well as the size of the formed thrombi, is comparable to each other (Figure 9). At the same time, the blood flow through the capillary was laminar and the speed constant. Abnormal aggregative (or other) activity was not observed. Similar results were obtained for unmodified and PSS-modified

nanoparticles (see Figure 9). By the end of the analysis, the thrombi reached comparable sizes, similar to the results of the control experiment.

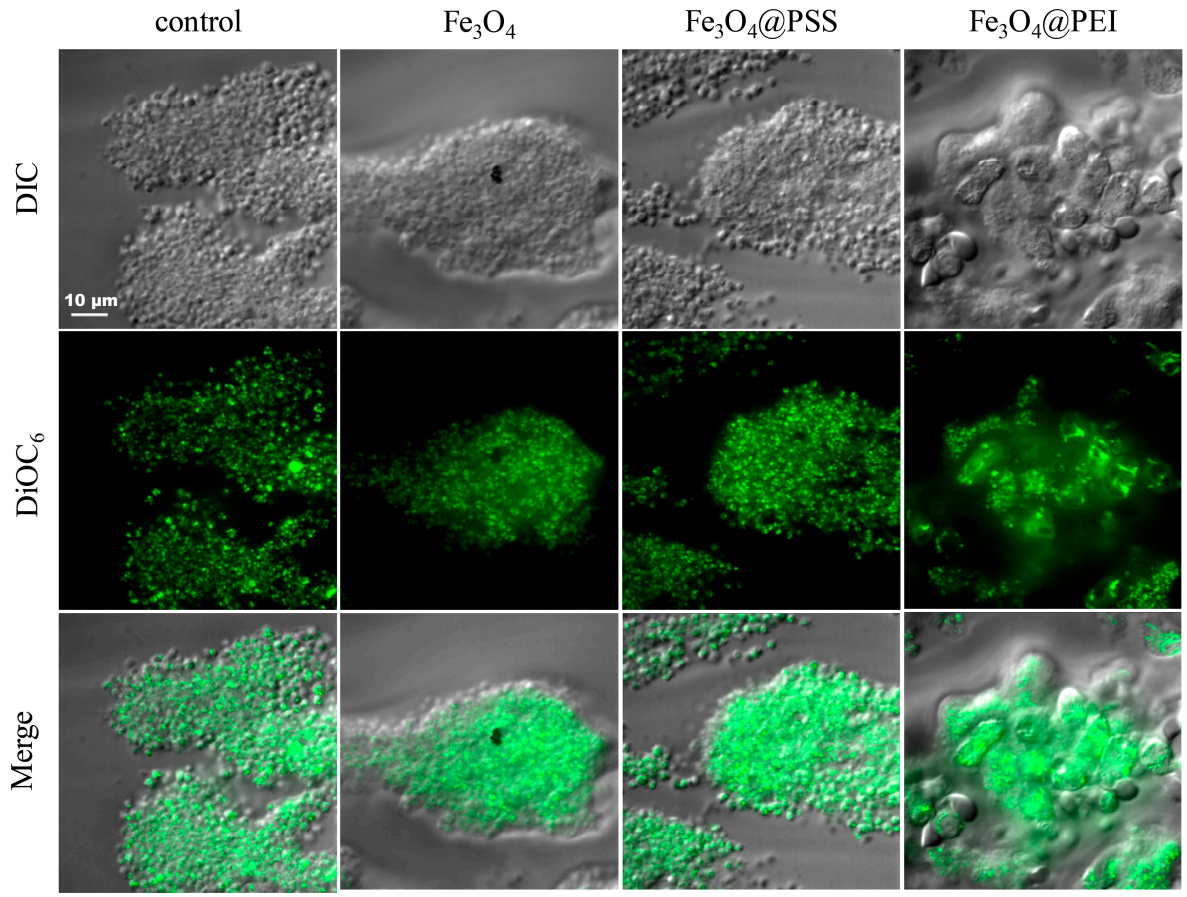


**Figure 9.** Micrographs of blood clots in the chamber in various shooting modes. DIC = differential interference contrast (optical microscope); $DiOC_6$ = cell-permeant lipophilic dye that is selective for the mitochondria of live cells (fluorescence microscopy); Merge = summarized image (optical and fluorescent microscopy).

Conversely, $Fe_3O_4$@PEI caused increased thrombus formation. The appearance of large aggregates of platelets and immune cells was already registered in the blood at the entrance to the flow chamber with collagen, which may indicate the effect of this sample type of particles on platelets. The morphology of the formed thrombi was visually different from other samples, and their size was much larger than in other cases.

## 3. Materials and Methods

### *3.1. Chemicals*

Iron(II) sulfate, ammonium chloride, 25% ammonia solution, and o-phosphoric acid were purchased from Reakhim (Moscow, Russia). Sodium hydroxide was obtained from LenReaktiv (St. Petersburg, Russia). 1,2-Propylene glycol was the product of EKOS-1 (Moscow, Russia). D-Glucose monohydrate was obtained from LenReaktiv (St. Petersburg, Russia). Anhydrous sodium hydrogen phosphate (≥99.0%) and potassium dihydrogen phosphate (≥99.5%) used to prepare the buffer solutions were purchased from Sigma-Aldrich (St. Louis, MO, USA). All chemicals were of analytical grade and were used as received. Dextran ($(C_6H_{10}O_5)_n$ $M_r$~40.000), sodium poly(4-styrenesulfonate) (PSS, $M_r$~70.000) and branched polyethylenimine (PEI, $M_r$~25,000) were obtained from Sigma-Aldrich, DOX (lyophilizate for solution for injection, 10 mg/ampoule) was obtained from Pharmachemie (Petah Tikva, Israel). All solutions were prepared using ultrapure water obtained from a Milli-Q system, Millipore Corporation (Millipore SAS, Molsheim, France).

### *3.2. Synthesis of IONs*

Cubic magnetite ($Fe_3O_4$) was obtained by precipitation followed by deposit aging in accordance with slightly modified published approach [141] (see Figure 10 for details). First, an alkaline solution was prepared by dissolving 3.86 g of NaOH in 400 mL of deionized water under nitrogen atmosphere. Then, a solution of iron(II) sulfate was made up by dissolving 10.0 g of $FeSO_4 \cdot 7H_2O$ in 100 mL of deionized water under nitrogen atmosphere. This solution was added to the NaOH solution heated to 80 °C and constantly stirred at 2000 rpm. Next, a current of air (1000 mL·min$^{-1}$) was passed through the mixed solution for 2 h, as a result the colloidal solution changed color from light blue to black. The resulting IONs were isolated from suspension by centrifugation (6000 rpm, 10 min), washed several times with deionized water and ethanol, and dispersed in propylene glycol under the action of ultrasound for 1 h. After heating at 180 °C for 3 h in a Teflon autoclave, the particles were cooled, washed with water and ethanol, and isolated by centrifugation (same conditions as above). The IONs were applied at a concentration of 100 µg·mL$^{-1}$ in all suspensions under investigation, unless stated otherwise.

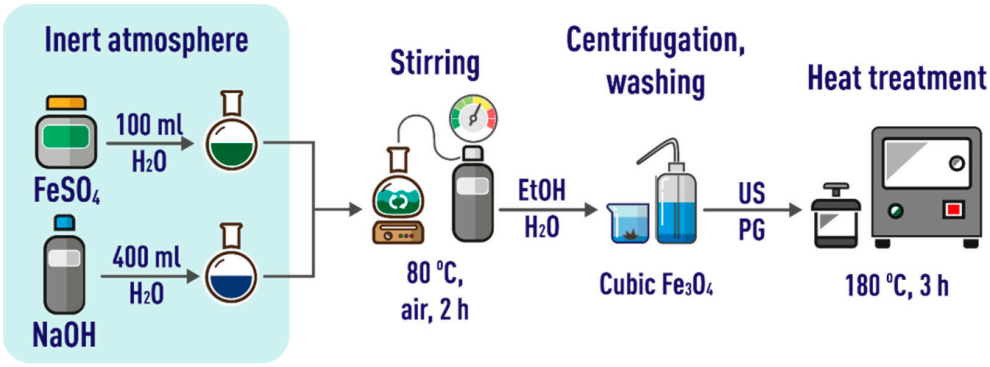


**Figure 10.** A workflow for obtaining nanoparticles of cubic magnetite. US = ultrasound; PG = propylene glycol.

### *3.3. Coating with Polyelectrolytes and Dextran*

An aqueous suspension of IONs was mixed with a respective modifier solution (100 µg·mL$^{-1}$) at a ratio of 1:10, sonicated for 10 min, and stirred for 24 h at 50 rpm. The modified particles were washed several times with water and ethanol and isolated by centrifugation at 4000 rpm (Figure 11).

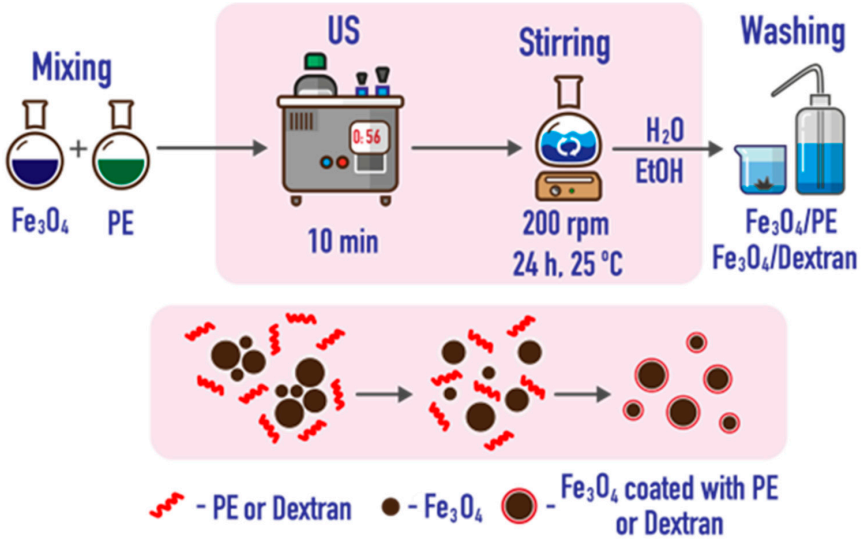


**Figure 11.** A scheme of modification of IONs with polyelectrolytes (PE) and dextran.

### *3.4. Coating with Porous Carbon*

Nanoparticles were coated with porous carbon (Carb) by hydrothermal carbonization in aqueous medium [117]. A total of 10 mL of an aqueous particle suspension (10 mg·mL$^{-1}$) was added to 20 mL of water containing 200 mg of glucose, at a ratio to saccharide as 1:2 by weight. The mixture was diluted with deionized water to 50 mL, stirred for 2 h and then sonicated for 20 min. The resulting suspension was quantitatively transferred to a Teflon autoclave, kept for 12 h at 180 °C, cooled, and washed several times with water and ethanol. Finally, the modified particles were separated by centrifugation at 4000 rpm (Figure 12).

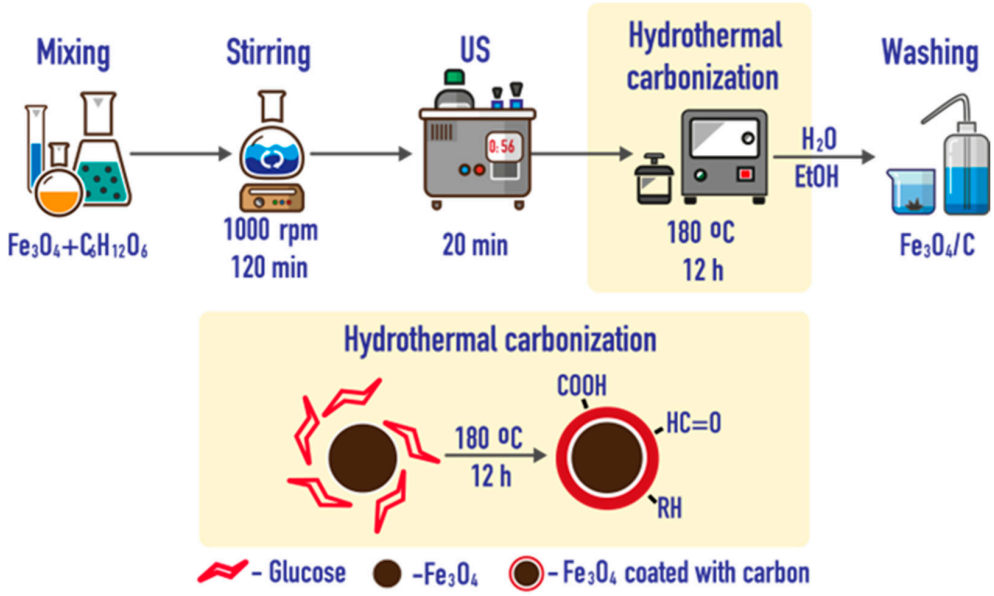


**Figure 12.** Synthesis of IONs coated with porous carbon.

### *3.5. Characterization of Nanoparticles*

The size and shape of nanoparticles were measured using a scanning electron microscope with a resolution of 1.2 nm at 30 keV, the VEGA 3 Tescan (Brno, Czech Republic) and the transmission electron microscope Tecnai-G2 F20 (FEI Company, Hillsboro, OR, USA) with a spatial resolution of up to 0.2 nm. Hydrodynamic diameter (z-average size) and surface charge (zeta-potential, $\zeta$) values of sample suspensions were recorded by dynamic light scattering (DLS) analysis using a Nano-ZS Zetasizer, model ZEN3600 (Malvern Instruments Ltd., Malvern, UK) at an angle of 173°. X-ray diffraction measurements were carried out on a Bruker D2 PHASER diffractometer (Bruker, Billerica, MA, USA) using Cu K$\alpha$ radiation ($\lambda$ = 0.154 nm) at 40 kV and 30 mA in the range of 2$\theta$ values (from 10° to 80°). Absorption and IR spectra were recorded with a Shimadzu UV-2550 spectrophotometer (Shimadzu, Kyoto, Japan) and a Bruker Vector 22 FTIR spectrometer (Bruker, Ettlingen, Germany), respectively. Magnetization curves were monitored using a Lake Shore 7407 magnetometer (Lake Shore Cryotronics Inc., Westville, IN, USA). The solutions were mixed on Bio RS-24 analog controlled rotator (BioSan, Riga, Latvia). Used for the magnetic separation was a permanent Nd–Fe–B magnet with $(VN)_{max}$ = 40 MGOe (Guangzhou, China). For dispersion and functionalization of IONs, a Grad 57–35 serial ultrasonic bath with a generator power of 165 W (Grad-Technology, Moscow, Russia) was used. For hydrothermal carbonization, a 50 mL Teflon autoclave with a Toption (Xi'an, China) stainless steel body was employed. Sedimentation analysis and sample centrifugation were performed, respectively, on an Vibra HT-224RCE analytical balance Shinko Denshi, Co. (Tokyo, Japan) and using an EBA 200 centrifuge (Hettich, Kirchlengern, Germany).

### *3.6. Sorption of DOX*

An analysis of the literature showed that the optimum conditions for the sorption of DOX correspond to neutral phosphate-buffered saline (PBS; Table S2). Polypropylene tubes were used for sorption, as previously recommended [42]. To assess the effect of sorption time, 5 mL of standard ION suspension and 5 mL of aqueous solution of doxorubicin (100 μg·mL$^{-1}$) were placed in each of six test tubes and the mixture was diluted to 30 mL with phosphate buffer solution at pH 7.4 (10 mmol·L$^{-1}$). The tubes were placed in a rotary mixer and stirred at 20 rpm. At certain time intervals (2, 5, 10, 15, 30, and 45 min), one test tube was removed and after the precipitation of IONs by applying an external magnetic field, the supernatant was separated to determine the unbound drug spectrophotometrically [142].

To assess the effect of the nanosorbent mass, 8 solutions were used, containing the same amount of doxorubicin (500 μg) and increasing amounts of IONs, from 0.5 to 50 mg (final volume 10 mL). The tubes were placed in a rotary mixer and stirred for 45 min at 20 rpm. The IONs were then magnetically separated and the concentration of DOX in the supernatant determined (Figure 13).

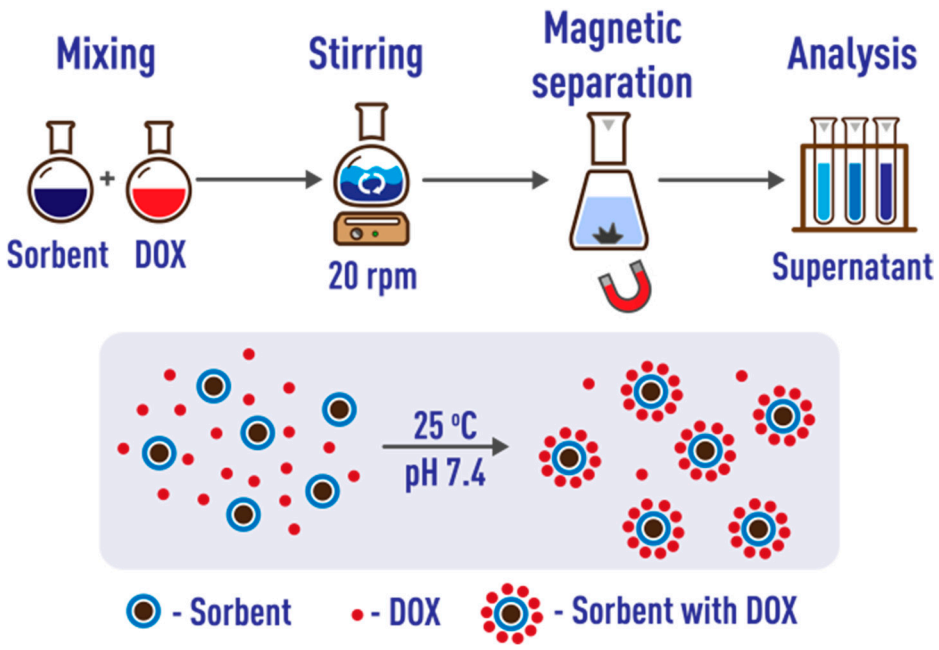


**Figure 13.** Exploring doxorubicin sorption on modified IONs. DOX = doxorubicin.

The degree of sorption was calculated as

$$R = \frac{(C_0 - C)}{C_0} \cdot 100\% \quad (1)$$

where $C_0$ is the initial concentration of the drug and $C$ is its residual concentration after sorption. To compare the efficiency of drug sorption by different sorbents, we used the sorption capacity calculated by the following equation:

$$q = \frac{(m_0 - m)_{DOX}}{m_S} \quad (2)$$

where $q$ is the difference between the initial ($m_0$) and residual ($m$) masses of DOX in solution and $m_S$ is the mass of the sorbent. Each experimental series was repeated at least five times.

We repeated the measurements three times and built graphs of the averaged values.

### 3.7. Adsorption Kinetics

To evaluate the adsorption kinetics, we used the pseudo-first-order and pseudo-second-order models [109] specified by the following equations:

$$q_t = q_e[1 - \exp(-k_1 t)] \quad (3)$$

and

$$q_t = \frac{q_e^2 k_2 t}{1 + q_e k_2 t} \quad (4)$$

where $q_t$ is the amount of adsorbed drug at time $t$ per 1 g of sorbent (mg·g$^{-1}$), $q_e$ is the equilibrium (maximum) amount of adsorbed drug per 1 g of sorbent (mg·g$^{-1}$), $k_1$ (min$^{-1}$), and $k_2$ (g·mg$^{-1}$·min$^{-1}$) are the pseudo-first and pseudo-second order constants, respectively.

### 3.8. Desorption of Doxorubicin

In the release studies, 5.0 mg of differently functionalized IONs with adsorbed drug were placed in 50 mL of phosphate buffer (pH 5.0 and 7.4) and mechanically stirred for 24 h at 20 rpm. At the pre-determined time points (5, 10, 15, 30, 60, 120, 360, and 1440 min), a 5 mL aliquot was removed, the supernatant was separated from the sorbent using a magnet and the doxorubicin concentration was determined by the spectrophotometric method. DOX releases were calculated using the following equation:

$$Cumulative\ release = \frac{m_t}{m_\infty} \cdot 100\% \quad (5)$$

where $m_t$ is the amount of released DOX at time $t$ and $m_\infty$ is the total amount of DOX loaded onto the sorbent.

Each experimental series was repeated at least three times and the averaged values were used to build graphs.

### 3.9. Cell Viability Analysis

Cell viability analysis was carried out according to the method described earlier [143], with slight changes.

#### 3.9.1. Cell Culture

Neuro-2A (N2A) cell lines (obtained from the American Type Culture Collection, ATCC, Manassas, VI, USA) were cultured in standard DMEM media (Biolot, St. Petersburg, Russia) supplemented with 10% fetal bovine serum (FBS; Gibco, Waltham, MA, USA), L-glutamine (Biolot), and 100 μg·mL$^{-1}$ penicillin/streptomycin (Biolot). The media were replaced every 3 days, and the cells were maintained in a humidified incubator (Innova CO-170, Hyland Scientific, Washington, DC, USA) at 5% $CO_2$ and 37 °C.

#### 3.9.2. Cell Viability

The effects of the nanoparticles on N2A cells were determined by the standard Alamar-Blue test. Cells were seeded into 96-well cell culture plates (Eppendorf, Hamburg, Germany) at a cell density of $10^4$/well in the culture medium and incubated at 37 °C under 5% $CO_2$ during 24 h. The particle solutions at concentrations 1, 5, 10, 50, and 100 μg·L$^{-1}$ were tested. After 24 h, 10 μL of the fluorescent dye AlamarBlue (10,000 U·mL$^{-1}$, Thermo Fisher Scientific, Waltham, MA, USA) was added to each well, and the fluorescence (540/590 nm) intensity was measured with a spectrophotometer (Infinite F200 PRO, Männedorf, Switzerland).

### 3.10. Real-Time Platelet Dynamics Ex Vivo Observed by Confocal Microscopy

The rate of thrombus formation in the presence of NPs was assessed according to a slightly modified method described in [144].

#### 3.10.1. Human Blood Collection

Human blood collection investigations were performed in accordance with the Declaration of Helsinki under a protocol approved by the NMRC PHOI Ethical Committee Informed written consent was obtained from all donors. Blood was collected in sterile tubes containing Hirudin anticoagulant (100 U·mL$^{-1}$; Merck, Darmstadt, Germany).

#### 3.10.2. Preparation of Flow Chamber System and Human Blood for Perfusion

Glass coverslips (24 × 24 mm; Heinz Herenz Medizinalbedarf GmbH, Hamburg, Germany) were cleaned with Plasma Cleaner (Harrick Plasma Inc, Ithaca, NY, USA). In order to immobilize collagen fibers on the surface of cleaned glass coverslips, we diluted stock solution of native Chronolog fibrillar type I collagen reagent (1 mg·mL$^{-1}$, Chrono-Log, Havertown, PA, USA), which already has collagen fibrils, with a 20 mM acetic acid (Reakhim) to a final concentration of collagen solution of 200 μg·mL$^{-1}$. This solution was added as a 10 μL drop to the surface of a cleaned glass coverslip and incubated for 40 min in a humid chamber at room temperature, then rinsed with water, dried, and assembled as part of the parallel platelet flow chamber described in [145]. Before perfusion, the fluorescent dye $DiOC_6(3)$ (3,3′-dihexyloxacarbocyanine iodide; Thermo Fisher Scientific) was added in an amount of 0.1% (final concentration 1 μM) of the blood volume and an aqueous dispersion of IONs (concentration 0.5 μg·μL$^{-1}$) in an amount of 1% of the blood volume.

#### 3.10.3. In Vitro Flow-Based Thrombus Formation Assay

Hirudinized (100 U·mL$^{-1}$) human whole blood in the presence of $DiOC_6(3)$ dye was perfused at a wall shear rate (1000 s$^{-1}$) through collagen-coated channels at room temperature using a programmable syringe pump PHD 2000 (Harvard Apparatus, Hollistion, MA, USA). $DiOC_6(3)$-loaded platelets were visualized by differential interferential contrast (DIC) or fluorescence microscopy with an Axio Observer Z1 microscope (Carl Zeiss, Jena, Germany) equipped with a 100× microscopic objective. Images were acquired with a Photometrics EMCCD camera (QuantEM 512sc, Teledyne Technologies, Thousand Oaks, CA, USA).

## 4. Conclusions

Thus, in this work, we functionalized the nanomagnetite surface with cationic (PEI), anionic (PSS), and nonionic (dextran, Dex) modifiers, as well as porous carbon (Carb), and compared the degree of loading of these and bare MNPs with doxorubicin. Using DLS and TEM, we found that the size of the obtained sorbents is in the range of 80–290 nm. We have shown that modification with polymers increases the stability of particles in aqueous suspension by a factor of 4–6 compared to unmodified magnetite. A comparison of the sorption capacity of MNPs with respect to DOX made it possible to establish the following series of sorption efficiency: $Fe_3O_4$@PEI (691) > $Fe_3O_4$@PSS (325) > $Fe_3O_4$@Carb (151) > $Fe_3O_4$@Dex (63) > $Fe_3O_4$ (45) mg g$^{-1}$. All samples showed no significant drug release (<7%) at pH 7.4, while at pH 5.0 the release rate and extent of desorption, although increased by 2–3 times, remained relatively low. The drug release percentage varies from 30 for $Fe_3O_4$@PSS to 13–16 for $Fe_3O_4$@Dex and $Fe_3O_4$@Carb, and up to about 6% for $Fe_3O_4$@PEI after a 30 min incubation at pH 5.0. Cytotoxicity analysis showed high biocompatibility of $Fe_3O_4$, $Fe_3O_4$@PSS, and $Fe_3O_4$@PEI. The survival rate of Neuro2A cells was above 80%. A preliminary assessment of the effect of unmodified and PSS-modified IONs on the rate of thrombus formation in the blood did not reveal noticeable changes. We believe that the obtained materials and results of the study can be taken into account when developing new drug delivery platforms.

**Supplementary Materials:** The following supporting information can be downloaded at https://www.mdpi.com/article/10.3390/ijms24054480/s1, References [9–12,17,21,33,36–38,41,42,44–47,50,53–55,57–59,61,62,66,75,78,82,114,120,124–126,128,129] are cited in the supplementary materials.

**Author Contributions:** Conceptualization, V.R.K.; methodology, V.R.K., M.R.C., S.I.O. and S.V.M.; validation, V.R.K., M.R.C. and S.I.O.; formal analysis, V.R.K.; resources, G.V.S. and S.N.S.; writing—original draft preparation, V.R.K., M.R.C. and S.I.O.; writing—review and editing, V.R.K. and S.N.S.; supervision, S.N.S.; project administration, S.N.S.; All authors have read and agreed to the published version of the manuscript.

**Funding:** This work was supported by the Russian Science Foundation (project 21-13-00267).

**Institutional Review Board Statement:** The study was performed in accordance with the Declaration of Helsinki under a protocol approved by the FRCC CHOI Ethical Committee.

**Informed Consent Statement:** Written informed consent has been obtained from all donors to publish this paper.

**Data Availability Statement:** Not applicable.

**Acknowledgments:** HRTEM experiments were effectuated using equipment of the "Nanochemistry and Nanomaterials" center supported by the Program of Development of Lomonosov Moscow State University".

**Conflicts of Interest:** The authors declare no conflict of interest.

## References

1. Tacar, O.; Sriamornsak, P.; Dass, C.R. Doxorubicin: An update on anticancer molecular action, toxicity and novel drug delivery systems. *J. Pharm. Pharmacol.* **2013**, *65*, 157–170. [CrossRef] [PubMed]
2. Sritharan, S.; Sivalingam, N. A comprehensive review on time-tested anticancer drug doxorubicin. *Life Sci.* **2021**, *278*, 119527. [CrossRef] [PubMed]
3. D'Angelo, N.A.; Noronha, M.A.; Câmara, M.C.C.; Kurnik, I.S.; Feng, C.; Araujo, V.H.S.; Santos, J.H.P.M.; Feitosa, V.; Molino, J.V.D.; Rangel-Yagui, C.O.; et al. Doxorubicin nanoformulations on therapy against cancer: An overview from the last 10 years. *Biomater. Adv.* **2022**, *133*, 112623. [CrossRef] [PubMed]
4. Kumar, A.; Gautam, B.; Dubey, C.; Tripathi, P.K. A review: Role of doxorubicin in treatment of cancer. *Int. J. Pharm. Sci. Res.* **2014**, *5*, 4117–4128. [CrossRef]
5. Damiani, R.M.; Moura, D.J.; Viau, C.M.; Caceres, R.A.; Henriques, J.A.P.; Saffi, J. Pathways of cardiac toxicity: Comparison between chemotherapeutic drugs doxorubicin and mitoxantrone. *Arch. Toxicol.* **2016**, *90*, 2063–2076. [CrossRef]
6. Renu, K.; Abilash, V.G.; Tirupathi Pichiah, P.B.; Arunachalam, S. Molecular mechanism of doxorubicin-induced cardiomyopathy—An update. *Eur. J. Pharmacol.* **2018**, *818*, 241–253. [CrossRef] [PubMed]
7. Akhtar, N.; Mohammed, H.A.; Yusuf, M.; Al-Subaiyel, A.; Sulaiman, G.M.; Khan, R.A. SPIONs Conjugate Supported Anticancer Drug Doxorubicin's Delivery: Current Status, Challenges, and Prospects. *Nanomaterials* **2022**, *12*, 3686. [CrossRef]
8. Kanwal, U.; Irfan Bukhari, N.; Ovais, M.; Abass, N.; Hussain, K.; Raza, A. Advances in nano-delivery systems for doxorubicin: An updated insight. *J. Drug Target.* **2018**, *26*, 296–310. [CrossRef]
9. AlHazmi, G.A.A.; AbouMelha, K.S.; El-Desouky, M.G.; El-Bindary, A.A. Effective adsorption of doxorubicin hydrochloride on zirconium metal-organic framework: Equilibrium, kinetic and thermodynamic studies. *J. Mol. Struct.* **2022**, *1258*, 132679. [CrossRef]
10. Abdelfattah, A.; Aboutaleb, A.E.; Abdel-Aal, A.B.M.; Abdellatif, A.A.H.; Tawfeek, H.M.; Abdel-Rahman, S.I. Design and optimization of PEGylated silver nanoparticles for efficient delivery of doxorubicin to cancer cells. *J. Drug Deliv. Sci. Technol.* **2022**, *71*, 103347. [CrossRef]
11. Kurdyukov, D.A.; Eurov, D.A.; Shmakov, S.V.; Kirilenko, D.A.; Kukushkina, J.A.; Smirnov, A.N.; Yagovkina, M.A.; Klimenko, V.V.; Koniakhin, S.V.; Golubev, V.G. Fabrication of doxorubicin-loaded monodisperse spherical micro-mesoporous silicon particles for enhanced inhibition of cancer cell proliferation. *Microporous Mesoporous Mater.* **2019**, *281*, 1–8. [CrossRef]
12. Abdelhalim, A.O.E.; Ageev, S.V.; Petrov, A.V.; Meshcheriakov, A.A.; Luttsev, M.D.; Vasina, L.V.; Nashchekina, I.A.; Murin, I.V.; Molchanov, O.E.; Maistrenko, D.N.; et al. Graphene oxide conjugated with doxorubicin: Synthesis, bioactivity, and biosafety. *J. Mol. Liq.* **2022**, *359*, 119156. [CrossRef]
13. Chadar, R.; Afzal, O.; Alqahtani, S.M.; Kesharwani, P. Carbon nanotubes as an emerging nanocarrier for the delivery of doxorubicin for improved chemotherapy. *Colloids Surf. B Biointerfaces* **2021**, *208*, 112044. [CrossRef] [PubMed]
14. Wang, Y.; Xu, Z. Interaction mechanism of doxorubicin and SWCNT: Protonation and diameter effects on drug loading and releasing. *RSC Adv.* **2016**, *6*, 314–322. [CrossRef] [PubMed]

15. Butowska, K.; Kozak, W.; Zdrowowicz, M.; Makurat, S.; Rychłowski, M.; Hać, A.; Herman-Antosiewicz, A.; Piosik, J.; Rak, J. Cytotoxicity of doxorubicin conjugated with C60 fullerene. Structural and in vitro studies. *Struct. Chem.* **2019**, *30*, 2327–2338. [CrossRef]
16. Sawy, A.M.; Barhoum, A.; Abdel Gaber, S.A.; El-Hallouty, S.M.; Shousha, W.G.; Maarouf, A.A.; Khalil, A.S.G. Insights of doxorubicin loaded graphene quantum dots: Synthesis, DFT drug interactions, and cytotoxicity. *Mater. Sci. Eng. C* **2021**, *122*, 111921. [CrossRef]
17. Xu, G.; Zhang, W.; Du, J.; Yuan, X.; Zhang, W.; Yan, W.; Liu, G. Biomass-derived porous carbon with high drug adsorption capacity undergoes enzymatic and chemical degradation. *J. Colloid Interface Sci.* **2022**, *622*, 87–96. [CrossRef]
18. Ma, Z.; Mohapatra, J.; Wei, K.; Liu, J.P.; Sun, S. Magnetic Nanoparticles: Synthesis, Anisotropy, and Applications. *Chem. Rev.* **2021**. [CrossRef]
19. Liu, S.; Yu, B.; Wang, S.; Shen, Y.; Cong, H. Preparation, surface functionalization and application of Fe3O4 magnetic nanoparticles. *Adv. Colloid Interface Sci.* **2020**, *281*, 102165. [CrossRef]
20. Nguyen, M.D.; Tran, H.-V.; Xu, S.; Lee, T.R. $Fe_3O_4$ Nanoparticles: Structures, Synthesis, Magnetic Properties, Surface Functionalization, and Emerging Applications. *Appl. Sci.* **2021**, *11*, 11301. [CrossRef]
21. Nigam, S.; Chandra, S.; Newgreen, D.F.; Bahadur, D.; Chen, Q. Poly(ethylene glycol)-Modified PAMAM-$Fe_3O_4$-Doxorubicin Triads with the Potential for Improved Therapeutic Efficacy: Generation-Dependent Increased Drug Loading and Retention at Neutral pH and Increased Release at Acidic pH. *Langmuir* **2014**, *30*, 1004–1011. [CrossRef] [PubMed]
22. Shen, L.; Li, B.; Qiao, Y. $Fe_3O_4$ Nanoparticles in Targeted Drug/Gene Delivery Systems. *Materials* **2018**, *11*, 324. [CrossRef] [PubMed]
23. Kuznetsova, O.V.; Reshetnikova, I.S.; Shtykov, S.N.; Karandashev, V.K.; Keppler, B.K.; Timerbaev, A.R. A simple assay for probing transformations of superparamagnetic iron oxide nanoparticles in human serum. *Chem. Commun.* **2019**, *55*, 4270–4272. [CrossRef] [PubMed]
24. Malhotra, N.; Lee, J.S.; Liman, R.A.D.; Ruallo, J.M.S.; Villaflores, O.B.; Ger, T.R.; Hsiao, C.D. Potential Toxicity of Iron Oxide Magnetic Nanoparticles: A Review. *Molecules* **2020**, *25*, 3159. [CrossRef] [PubMed]
25. Mehta, R.V. Synthesis of magnetic nanoparticles and their dispersions with special reference to applications in biomedicine and biotechnology. *Mater. Sci. Eng. C* **2017**, *79*, 901–916. [CrossRef] [PubMed]
26. Samrot, A.V.; Sahithya, C.S.; Selvarani A, J.; Purayil, S.K.; Ponnaiah, P. A review on synthesis, characterization and potential biological applications of superparamagnetic iron oxide nanoparticles. *Curr. Res. Green Sustain. Chem.* **2021**, *4*, 100042. [CrossRef]
27. Abd Elrahman, A.A.; Mansour, F.R. Targeted magnetic iron oxide nanoparticles: Preparation, functionalization and biomedical application. *J. Drug Deliv. Sci. Technol.* **2019**, *52*, 702–712. [CrossRef]
28. Petrov, K.D.; Chubarov, A.S. Magnetite Nanoparticles for Biomedical Applications. *Encyclopedia* **2022**, *2*, 1811–1828. [CrossRef]
29. Popescu, R.C.; Andronescu, E.; Grumezescu, A.M. In vivo evaluation of $Fe_3O_4$ nanoparticles. *Rom. J. Morphol. Embryol. Rev. Roum. Morphol. Embryol.* **2014**, *55*, 1013–1018.
30. Gobbo, O.L.; Sjaastad, K.; Radomski, M.W.; Volkov, Y.; Prina-Mello, A. Magnetic Nanoparticles in Cancer Theranostics. *Theranostics* **2015**, *5*, 1249–1263. [CrossRef]
31. Zhu, L.; Zhou, Z.; Mao, H.; Yang, L. Magnetic nanoparticles for precision oncology: Theranostic magnetic iron oxide nanoparticles for image-guided and targeted cancer therapy. *Nanomedicine* **2016**, *12*, 73–87. [CrossRef] [PubMed]
32. Su, D.; Wu, K.; Saha, R.; Liu, J.; Wang, J.-P. Magnetic nanotechnologies for early cancer diagnostics with liquid biopsies: A review. *J. Cancer Metastasis Treat.* **2020**, *6*, 19. [CrossRef]
33. Eslami, P.; Albino, M.; Scavone, F.; Chiellini, F.; Morelli, A.; Baldi, G.; Cappiello, L.; Doumett, S.; Lorenzi, G.; Ravagli, C.; et al. Smart Magnetic Nanocarriers for Multi-Stimuli On-Demand Drug Delivery. *Nanomaterials* **2022**, *12*, 303. [CrossRef] [PubMed]
34. Vangijzegem, T.; Lecomte, V.; Ternad, I.; Van Leuven, L.; Muller, R.N.; Stanicki, D.; Laurent, S. Superparamagnetic Iron Oxide Nanoparticles (SPION): From Fundamentals to State-of-the-Art Innovative Applications for Cancer Therapy. *Pharmaceutics* **2023**, *15*, 236. [CrossRef]
35. Demin, A.M.; Vakhrushev, A.V.; Pershina, A.G.; Valova, M.S.; Efimova, L.V.; Syomchina, A.A.; Uimin, M.A.; Minin, A.S.; Levit, G.L.; Krasnov, V.P.; et al. Magnetic-Responsive Doxorubicin-Containing Materials Based on $Fe_3O_4$ Nanoparticles with a $SiO_2$/PEG Shell and Study of Their Effects on Cancer Cell Lines. *Int. J. Mol. Sci.* **2022**, *23*, 9093. [CrossRef]
36. Le, T.T.H.; Bui, T.Q.; Ha, T.M.T.; Le, M.H.; Pham, H.N.; Ha, P.T. Optimizing the alginate coating layer of doxorubicin-loaded iron oxide nanoparticles for cancer hyperthermia and chemotherapy. *J. Mater. Sci.* **2018**, *53*, 13826–13842. [CrossRef]
37. Yang, Y.; Guo, Q.; Peng, J.; Su, J.; Lu, X.; Zhao, Y.; Qian, Z. Doxorubicin-Conjugated Heparin-Coated Superparamagnetic Iron Oxide Nanoparticles for Combined Anticancer Drug Delivery and Magnetic Resonance Imaging. *J. Biomed. Nanotechnol.* **2016**, *12*, 1963–1974. [CrossRef]
38. Chandra, S.; Mehta, S.; Nigam, S.; Bahadur, D. Dendritic magnetite nanocarriers for drug delivery applications. *New J. Chem.* **2010**, *34*, 648–655. [CrossRef]
39. Zhu, N.; Ji, H.; Yu, P.; Niu, J.; Farooq, M.U.; Akram, M.W.; Udego, I.O.; Li, H.; Niu, X. Surface Modification of Magnetic Iron Oxide Nanoparticles. *Nanomaterials* **2018**, *8*, 810. [CrossRef]
40. Gao, Q.; Xie, W.; Wang, Y.; Wang, D.; Guo, Z.; Gao, F.; Zhao, L.; Cai, Q. A theranostic nanocomposite system based on radial mesoporous silica hybridized with $Fe_3O_4$ nanoparticles for targeted magnetic field responsive chemotherapy of breast cancer. *RSC Adv.* **2018**, *8*, 4321–4328. [CrossRef]

41. Hernandes, E.P.; Bini, R.D.; Endo, K.M.; de Oliveira Junior, V.A.; de Almeida, I.V.; Dias, G.S.; dos Santos, I.A.; de Oliveira, P.N.; Vicentini, V.E.; Cotica, L.F. Doxorubicin-Loaded Magnetic Nanoparticles: Enhancement of Doxorubicin's Effect on Breast Cancer Cells (MCF-7). *Magnetochemistry* **2022**, *8*, 114. [CrossRef]
42. Demin, A.M.; Vakhrushev, A.V.; Valova, M.S.; Korolyova, M.A.; Uimin, M.A.; Minin, A.S.; Pozdina, V.A.; Byzov, I.V.; Tumashov, A.A.; Chistyakov, K.A.; et al. Effect of the Silica–Magnetite Nanocomposite Coating Functionalization on the Doxorubicin Sorption/Desorption. *Pharmaceutics* **2022**, *14*, 2271. [CrossRef]
43. Khani, T.; Alamzadeh, Z.; Sarikhani, A.; Mousavi, M.; Mirrahimi, M.; Tabei, M.; Irajirad, R.; Abed, Z.; Beik, J. $Fe_3O_4$@Au core–shell hybrid nanocomposite for MRI-guided magnetic targeted photo-chemotherapy. *Lasers Med. Sci.* **2022**, *37*, 2387–2395. [CrossRef]
44. Liu, X.; Wang, C.; Wang, X.; Tian, C.; Shen, Y.; Zhu, M. A dual-targeting $Fe_3O_4$@C/ZnO-DOX-FA nanoplatform with pH-responsive drug release and synergetic chemo-photothermal antitumor in vitro and in vivo. *Mater. Sci. Eng. C* **2021**, *118*, 111455. [CrossRef] [PubMed]
45. Cai, W.; Guo, M.; Weng, X.; Zhang, W.; Chen, Z. Adsorption of doxorubicin hydrochloride on glutaric anhydride functionalized $Fe_3O_4$@$SiO_2$ magnetic nanoparticles. *Mater. Sci. Eng. C* **2019**, *98*, 65–73. [CrossRef]
46. Singh, N.; Nayak, J.; Sahoo, S.K.; Kumar, R. Glutathione conjugated superparamagnetic $Fe_3O_4$-Au core shell nanoparticles for pH controlled release of DOX. *Mater. Sci. Eng. C* **2019**, *100*, 453–465. [CrossRef] [PubMed]
47. Qi, C.; Wang, W.; Wang, P.; Cheng, H.; Wang, X.; Gong, B.; Xie, A.; Shen, Y. Facile Synthesis of $Fe_3O_4$@Au/PPy-DOX Nanoplatform with Enhanced Glutathione Depletion and Controllable Drug Delivery for Enhanced Cancer Therapeutic Efficacy. *Molecules* **2022**, *27*, 4003. [CrossRef] [PubMed]
48. Piehler, S.; Dähring, H.; Grandke, J.; Göring, J.; Couleaud, P.; Aires, A.; Cortajarena, A.L.; Courty, J.; Latorre, A.; Somoza, Á.; et al. Iron Oxide Nanoparticles as Carriers for DOX and Magnetic Hyperthermia after Intratumoral Application into Breast Cancer in Mice: Impact and Future Perspectives. *Nanomaterials* **2020**, *10*, 1016. [CrossRef] [PubMed]
49. Nigam, S.; Barick, K.C.; Bahadur, D. Development of citrate-stabilized $Fe_3O_4$ nanoparticles: Conjugation and release of doxorubicin for therapeutic applications. *J. Magn. Magn. Mater.* **2011**, *323*, 237–243. [CrossRef]
50. Kovrigina, E.; Chubarov, A.; Dmitrienko, E. High Drug Capacity Doxorubicin-Loaded Iron Oxide Nanocomposites for Cancer Therapy. *Magnetochemistry* **2022**, *8*, 54. [CrossRef]
51. Han, Q.; Wang, X.; Sun, Z.; Xu, X.; Jin, L.; Qiao, L.; Yuan, Q. Rational design of $Fe_3O_4$@C nanoparticles for simultaneous bimodal imaging and chemo-photothermal therapy in vitro and in vivo. *J. Mater. Chem. B* **2018**, *6*, 5443–5450. [CrossRef] [PubMed]
52. Aram, E.; Moeni, M.; Abedizadeh, R.; Sabour, D.; Sadeghi-Abandansari, H.; Gardy, J.; Hassanpour, A. Smart and Multi-Functional Magnetic Nanoparticles for Cancer Treatment Applications: Clinical Challenges and Future Prospects. *Nanomaterials* **2022**, *12*, 3567. [CrossRef]
53. Javid, A.; Ahmadian, S.; Saboury, A.A.; Kalantar, S.M.; Rezaei-Zarchi, S.; Shahzad, S. Biocompatible APTES–PEG Modified Magnetite Nanoparticles: Effective Carriers of Antineoplastic Agents to Ovarian Cancer. *Appl. Biochem. Biotechnol.* **2014**, *173*, 36–54. [CrossRef] [PubMed]
54. Shen, C.; Wang, X.; Zheng, Z.; Gao, C.; Chen, X.; Zhao, S.; Dai, Z. Doxorubicin and indocyanine green loaded superparamagnetic iron oxide nanoparticles with PEGylated phospholipid coating for magnetic resonance with fluorescence imaging and chemotherapy of glioma. *Int. J. Nanomed.* **2019**, *14*, 101–117. [CrossRef]
55. Omidirad, R.; Rajabi Hosseinpour, F.; Farahani, B. Preparation and in vitro drug delivery response of doxorubicin loaded PAA coated magnetite nanoparticles. *J. Serb. Chem. Soc.* **2013**, *78*, 1609–1616. [CrossRef]
56. Jamal Al Dine, E.; Ferjaoui, Z.; Ghanbaja, J.; Roques-Carmes, T.; Meftah, A.; Hamieh, T.; Toufaily, J.; Schneider, R.; Marchal, S.; Gaffet, E.; et al. Thermo-responsive magnetic $Fe_3O_4$@P(MEO2MAX-OEGMA100-X) NPs and their applications as drug delivery systems. *Int. J. Pharm.* **2017**, *532*, 738–747. [CrossRef]
57. Akbarzadeh, A.; Samiei, M.; Joo, S.W.; Anzaby, M.; Hanifehpour, Y.; Nasrabadi, H.T.; Davaran, S. RETRACTED ARTICLE: Synthesis, characterization and in vitro studies of doxorubicin-loaded magnetic nanoparticles grafted to smart copolymers on A549 lung cancer cell line. *J. Nanobiotechnol.* **2012**, *10*, 46. [CrossRef] [PubMed]
58. Dutta, S.; Parida, S.; Maiti, C.; Banerjee, R.; Mandal, M.; Dhara, D. Polymer grafted magnetic nanoparticles for delivery of anticancer drug at lower pH and elevated temperature. *J. Colloid Interface Sci.* **2016**, *467*, 70–80. [CrossRef]
59. Rouhollah, K.; Pelin, M.; Serap, Y.; Gozde, U.; Ufuk, G. Doxorubicin Loading, Release, and Stability of Polyamidoamine Dendrimer-Coated Magnetic Nanoparticles. *J. Pharm. Sci.* **2013**, *102*, 1825–1835. [CrossRef]
60. Hayashi, K.; Nakamura, M.; Miki, H.; Ozaki, S.; Abe, M.; Matsumoto, T.; Sakamoto, W.; Yogo, T.; Ishimura, K. Magnetically responsive smart nanoparticles for cancer treatment with a combination of magnetic hyperthermia and remote-control drug release. *Theranostics* **2014**, *4*, 834–844. [CrossRef]
61. Liang, P.C.; Chen, Y.C.; Chiang, C.F.; Mo, L.R.; Wei, S.Y.; Hsieh, W.Y.; Lin, W.L. Doxorubicin-modified magnetic nanoparticles as a drug delivery system for magnetic resonance imaging-monitoring magnet-enhancing tumor chemotherapy. *Int. J. Nanomed.* **2016**, *11*, 2021–2037. [CrossRef]
62. Nogueira, J.; Soares, S.F.; Amorim, C.O.; Amaral, J.S.; Silva, C.; Martel, F.; Trindade, T.; Daniel-da-Silva, A.L. Magnetic Driven Nanocarriers for pH-Responsive Doxorubicin Release in Cancer Therapy. *Molecules* **2020**, *25*, 333. [CrossRef] [PubMed]
63. Hamidian, H.; Tavakoli, T. Preparation of a new $Fe_3O_4$/starch-g-polyester nanocomposite hydrogel and a study on swelling and drug delivery properties. *Carbohydr. Polym.* **2016**, *144*, 140–148. [CrossRef] [PubMed]

64. Movagharnegad, N.; Najafi Moghadam, P.; Nikoo, A.; Shokri, Z. Modification of Magnetite Cellulose Nanoparticles via Click Reaction for use in Controlled Drug Delivery. *Polym. Plast. Technol. Eng.* **2018**, *57*, 1915–1922. [CrossRef]
65. Adimoolam, M.G.; Amreddy, N.; Nalam, M.R.; Sunkara, M.V. A simple approach to design chitosan functionalized $Fe_3O_4$ nanoparticles for pH responsive delivery of doxorubicin for cancer therapy. *J. Magn. Magn. Mater.* **2018**, *448*, 199–207. [CrossRef]
66. Javid, A.; Ahmadian, S.; Saboury, A.A.; Kalantar, S.M.; Rezaei-Zarchi, S. Chitosan-Coated Superparamagnetic Iron Oxide Nanoparticles for Doxorubicin Delivery: Synthesis and Anticancer Effect Against Human Ovarian Cancer Cells. *Chem. Biol. Drug Des.* **2013**, *82*, 296–306. [CrossRef]
67. Mohammadi, R.; Saboury, A.; Javanbakht, S.; Foroutan, R.; Shaabani, A. Carboxymethylcellulose/polyacrylic acid/starch-modified $Fe_3O_4$ interpenetrating magnetic nanocomposite hydrogel beads as pH-sensitive carrier for oral anticancer drug delivery system. *Eur. Polym. J.* **2021**, *153*, 110500. [CrossRef]
68. Abbasian, M.; Mahmoodzadeh, F.; Khalili, A.; Salehi, R. Chemotherapy of Breast Cancer Cells Using Novel pH-Responsive Cellulose-Based Nanocomposites. *Adv. Pharm. Bull.* **2019**, *9*, 122–131. [CrossRef]
69. Liu, Q.; Tan, Z.; Zheng, D.; Qiu, X. pH-responsive magnetic $Fe_3O_4$/carboxymethyl chitosan/aminated lignosulfonate nanoparticles with uniform size for targeted drug loading. *Int. J. Biol. Macromol.* **2023**, *225*, 1182–1192. [CrossRef]
70. Mahdi Eshaghi, M.; Pourmadadi, M.; Rahdar, A.; Diez-Pascual, A.M. Novel Carboxymethyl Cellulose-Based Hydrogel with Core-Shell $Fe_3O_4$@$SiO_2$ Nanoparticles for Quercetin Delivery. *Materials* **2022**, *15*, 8711. [CrossRef]
71. Obireddy, S.R.; Lai, W.F. ROS-Generating Amine-Functionalized Magnetic Nanoparticles Coupled with Carboxymethyl Chitosan for pH-Responsive Release of Doxorubicin. *Int. J. Nanomed.* **2022**, *17*, 589–601. [CrossRef] [PubMed]
72. Huang, C.-H.; Chuang, T.-J.; Ke, C.-J.; Yao, C.-H. Doxorubicin–Gelatin/$Fe_3O_4$–Alginate Dual-Layer Magnetic Nanoparticles as Targeted Anticancer Drug Delivery Vehicles. *Polymers* **2020**, *12*, 1747. [CrossRef] [PubMed]
73. Khaliq, N.U.; Park, D.Y.; Lee, H.J.; Oh, K.S.; Seo, J.H.; Kim, S.Y.; Hwang, C.S.; Lim, T.-H.; Yuk, S.H. Pluronic/Heparin Nanoparticles for Chemo-Photodynamic Combination Cancer Therapy through Photoinduced Caspase-3 Activation. *ACS Appl. Nano Mater.* **2018**, *1*, 2943–2952. [CrossRef]
74. Nguyen, D.H. Heparin-Pluronic Coated Magnetic Nanoparticles for Doxorubicin Delivery. *JSM Nanotechnol. Nanomed.* **2017**, *5*, 1054. [CrossRef]
75. Javid, A.; Ahmadian, S.; Saboury, A.A.; Kalantar, S.M.; Rezaei-Zarchi, S. Novel biodegradable heparin-coated nanocomposite system for targeted drug delivery. *RSC Adv.* **2014**, *4*, 13719–13728. [CrossRef]
76. Toro-Cordova, A.; Llaguno-Munive, M.; Jurado, R.; Garcia-Lopez, P. The Therapeutic Potential of Chemo/Thermotherapy with Magnetoliposomes for Cancer Treatment. *Pharmaceutics* **2022**, *14*, 2443. [CrossRef]
77. Cardoso, B.D.; Rodrigues, A.R.O.; Bañobre-López, M.; Almeida, B.G.; Amorim, C.O.; Amaral, V.S.; Coutinho, P.J.G.; Castanheira, E.M.S. Magnetoliposomes Based on Shape Anisotropic Calcium/Magnesium Ferrite Nanoparticles as Nanocarriers for Doxorubicin. *Pharmaceutics* **2021**, *13*, 1248. [CrossRef]
78. Azlegini, A.; Javadpor, S.; Bahrolom, M. Liposome-$Fe_3O_4$-Doxorubicin Mediated Treatment of Melanoma Tumors. *Adv. Pharm. Bull.* 2022. [CrossRef]
79. Park, T.; Amatya, R.; Min, K.A.; Shin, M.C. Liposomal Iron Oxide Nanoparticles Loaded with Doxorubicin for Combined Chemo-Photothermal Cancer Therapy. *Pharmaceutics* **2023**, *15*, 292. [CrossRef]
80. Nitica, S.; Fizesan, I.; Dudric, R.; Loghin, F.; Lucaciu, C.M.; Iacovita, C. Doxorubicin Loaded Thermosensitive Magneto-Liposomes Obtained by a Gel Hydration Technique: Characterization and In Vitro Magneto-Chemotherapeutic Effect Assessment. *Pharmaceutics* **2022**, *14*, 2501. [CrossRef]
81. Edyta, M.; Paweł, K.; Michał, C. Perspective Chapter: Magnetoliposomes—A Recent Development as Recent Advances in the Field of Controlled Release Drug Delivery. In *Liposomes—Recent Advances, New Perspectives and Applications*; Rajeev, K.T., Ed.; IntechOpen: Rijeka, Croatia, 2022; p. Ch. 3.
82. Chakraborty, D.; Chauhan, P.; Kumar, S.; Chaudhary, S.; Chandrasekaran, N.; Mukherjee, A.; Ethiraj, K.R. Utilizing corona on functionalized selenium nanoparticles for loading and release of doxorubicin payload. *J. Mol. Liq.* **2019**, *296*, 111864. [CrossRef]
83. Flores-Rojas, G.G.; López-Saucedo, F.; Vera-Graziano, R.; Mendizabal, E.; Bucio, E. Magnetic Nanoparticles for Medical Applications: Updated Review. *Macromol* **2022**, *2*, 374–390. [CrossRef]
84. Mosayebi, J.; Kiyasatfar, M.; Laurent, S. Synthesis, Functionalization, and Design of Magnetic Nanoparticles for Theranostic Applications. *Adv. Healthc. Mater.* **2017**, *6*, 1700306. [CrossRef] [PubMed]
85. Anderson, S.D.; Gwenin, V.V.; Gwenin, C.D. Magnetic Functionalized Nanoparticles for Biomedical, Drug Delivery and Imaging Applications. *Nanoscale Res. Lett.* **2019**, *14*, 188. [CrossRef]
86. Khizar, S.; Ahmad, N.M.; Zine, N.; Jaffrezic-Renault, N.; Errachid-el-salhi, A.; Elaissari, A. Magnetic Nanoparticles: From Synthesis to Theranostic Applications. *ACS Appl. Nano Mater.* **2021**, *4*, 4284–4306. [CrossRef]
87. Huang, K.; Ma, H.; Liu, J.; Huo, S.; Kumar, A.; Wei, T.; Zhang, X.; Jin, S.; Gan, Y.; Wang, P.C.; et al. Size-Dependent Localization and Penetration of Ultrasmall Gold Nanoparticles in Cancer Cells, Multicellular Spheroids, and Tumors in Vivo. *ACS Nano* **2012**, *6*, 4483–4493. [CrossRef]
88. Guo, X.; Wu, Z.; Li, W.; Wang, Z.; Li, Q.; Kong, F.; Zhang, H.; Zhu, X.; Du, Y.P.; Jin, Y.; et al. Appropriate Size of Magnetic Nanoparticles for Various Bioapplications in Cancer Diagnostics and Therapy. *ACS Appl. Mater. Interfaces* **2016**, *8*, 3092–3106. [CrossRef]

89. Albanese, A.; Tang, P.S.; Chan, W.C.W. The Effect of Nanoparticle Size, Shape, and Surface Chemistry on Biological Systems. *Annu. Rev. Biomed. Eng.* **2012**, *14*, 1–16. [CrossRef]
90. Abaeva, A.A.; Canault, M.; Kotova, Y.N.; Obydennyy, S.I.; Yakimenko, A.O.; Podoplelova, N.A.; Kolyadko, V.N.; Chambost, H.; Mazurov, A.V.; Ataullakhanov, F.I.; et al. Procoagulant Platelets Form an α-Granule Protein-covered "Cap" on Their Surface That Promotes Their Attachment to Aggregates. *J. Biol. Chem.* **2013**, *288*, 29621–29632. [CrossRef]
91. Khoshnam, M.; Salimijazi, H. Synthesis and characterization of magnetic-photocatalytic $Fe_3O_4/SiO_2$/a-$Fe_2O_3$ nano core-shell. *Surf. Interfaces* **2021**, *26*, 101322. [CrossRef]
92. Cai, H.; An, X.; Cui, J.; Li, J.; Wen, S.; Li, K.; Shen, M.; Zheng, L.; Zhang, G.; Shi, X. Facile Hydrothermal Synthesis and Surface Functionalization of Polyethyleneimine-Coated Iron Oxide Nanoparticles for Biomedical Applications. *ACS Appl. Mater. Interfaces* **2013**, *5*, 1722–1731. [CrossRef]
93. Tang, X.; Sun, A.; Chu, C.; Wang, C.; Liu, Z.; Guo, J.; Xu, G. Highly sensitive multiresponsive photonic hydrogels based on a crosslinked Acrylamide- N-isopropylacrylamide (AM-NIPAM) co-polymer containing $Fe_3O_4$@C crystalline colloidal arrays. *Sens. Actuators B Chem.* **2016**, *236*, 399–407. [CrossRef]
94. Bagheri, S.; Esrafili, A.; Kermani, M.; Mehralipour, J.; Gholami, M. Performance evaluation of a novel rGO-$Fe_0/Fe_3O_4$-PEI nanocomposite for lead and cadmium removal from aqueous solutions. *J. Mol. Liq.* **2020**, *320*, 114422. [CrossRef]
95. Zhang, S.; Wang, Z.; Chen, H.; Kai, C.; Jiang, M.; Wang, Q.; Zhou, Z. Polyethylenimine functionalized $Fe_3O_4$/steam-exploded rice straw composite as an efficient adsorbent for Cr(VI) removal. *Appl. Surf. Sci.* **2018**, *440*, 1277–1285. [CrossRef]
96. Grenda, K.; Idström, A.; Evenäs, L.; Persson, M.; Holmberg, K.; Bordes, R. An analytical approach to elucidate the architecture of polyethyleneimines. *J. Appl. Polym. Sci.* **2022**, *139*, 51657. [CrossRef]
97. Xia, T.; Guan, Y.; Yang, M.; Xiong, W.; Wang, N.; Zhao, S.; Guo, C. Synthesis of polyethylenimine modified $Fe_3O_4$ nanoparticles with immobilized $Cu^{2+}$ for highly efficient proteins adsorption. *Colloids Surf. A Physicochem. Eng. Asp.* **2014**, *443*, 552–559. [CrossRef]
98. Imran, M.; Zouli, N.; Ahamad, T.; Alshehri, S.M.; Chandan, M.R.; Hussain, S.; Aziz, A.; Dar, M.A.; Khan, A. Carbon-coated $Fe_3O_4$ core–shell super-paramagnetic nanoparticle-based ferrofluid for heat transfer applications. *Nanoscale Adv.* **2021**, *3*, 1962–1975. [CrossRef]
99. Sevilla, M.; Fuertes, A.B. Chemical and Structural Properties of Carbonaceous Products Obtained by Hydrothermal Carbonization of Saccharides. *Chem.-A Eur. J.* **2009**, *15*, 4195–4203. [CrossRef]
100. Zhang, X.; Wang, J. Preparation of carbon coated $Fe_3O_4$ nanoparticles for magnetic separation of uranium. *Solid State Sci.* **2018**, *75*, 14–20. [CrossRef]
101. Zhang, C.; Shi, X.; Yu, F.; Quan, Y. Preparation of dummy molecularly imprinted polymers based on dextran-modified magnetic nanoparticles $Fe_3O_4$ for the selective detection of acrylamide in potato chips. *Food Chem.* **2020**, *317*, 126431. [CrossRef]
102. Hong, R.Y.; Feng, B.; Chen, L.L.; Liu, G.H.; Li, H.Z.; Zheng, Y.; Wei, D.G. Synthesis, characterization and MRI application of dextran-coated $Fe_3O_4$ magnetic nanoparticles. *Biochem. Eng. J.* **2008**, *42*, 290–300. [CrossRef]
103. Sakaguchi, M.; Makino, M.; Ohura, T.; Yamamoto, K.; Enomoto, Y.; Takase, H. Surface modification of $Fe_3O_4$ nanoparticles with dextran via a coupling reaction between naked $Fe_3O_4$ mechano-cation and naked dextran mechano-anion: A new mechanism of covalent bond formation. *Adv. Powder Technol.* **2019**, *30*, 795–806. [CrossRef]
104. Sugumaran, A.; Sadhasivam, J.; Gawas, P.; Nutalapati, V.; Pandian, R.; Kumar Perumal, S. Curcumin conjugated dextran coated $Fe_3O_4$ Nanoparticles: Cytotoxic effect on lung cancer cell line A549. *Mater. Sci. Eng. B* **2022**, *286*, 116047. [CrossRef]
105. Katagiri, K.; Matsuda, A.; Caruso, F. Effect of UV−Irradiation on Polyelectrolyte Multilayered Films and Hollow Capsules Prepared by Layer-by-Layer Assembly. *Macromolecules* **2006**, *39*, 8067–8074. [CrossRef]
106. Göktepe, F.; Bozkurt, A.; Günday, Ş.T. Synthesis and proton conductivity of poly(styrene sulfonic acid)/heterocycle-based membranes. *Polym. Int.* **2008**, *57*, 133–138. [CrossRef]
107. Wang, Z.-S.; Sasaki, T.; Muramatsu, M.; Ebina, Y.; Tanaka, T.; Wang; Watanabe, M. Self-Assembled Multilayers of Titania Nanoparticles and Nanosheets with Polyelectrolytes. *Chem. Mater.* **2003**, *15*, 807–812. [CrossRef]
108. Bansal, R.; Singh, R.; Kaur, K. Quantitative analysis of doxorubicin hydrochloride and arterolane maleate by mid IR spectroscopy using transmission and reflectance modes. *BMC Chem.* **2021**, *15*, 27. [CrossRef]
109. Lin, C.-R.; Ivanova, O.S.; Edelman, I.S.; Knyazev, Y.V.; Zharkov, S.M.; Petrov, D.A.; Sokolov, A.E.; Svetlitsky, E.S.; Velikanov, D.A.; Solovyov, L.A.; et al. Carbon Double Coated $Fe_3O_4$@C@C Nanoparticles: Morphology Features, Magnetic Properties, Dye Adsorption. *Nanomaterials* **2022**, *12*, 376. [CrossRef]
110. Songsurang, K.; Praphairaksit, N.; Siraleartmukul, K.; Muangsin, N. Electrospray fabrication of doxorubicin-chitosan-tripolyphosphate nanoparticles for delivery of doxorubicin. *Arch. Pharmacal Res.* **2011**, *34*, 583–592. [CrossRef]
111. Hadadian, Y.; Masoomi, H.; Dinari, A.; Ryu, C.; Hwang, S.; Kim, S.; Cho, B.k.; Lee, J.Y.; Yoon, J. From Low to High Saturation Magnetization in Magnetite Nanoparticles: The Crucial Role of the Molar Ratios Between the Chemicals. *ACS Omega* **2022**, *7*, 15996–16012. [CrossRef]
112. Kumar, A.; Dixit, C.K. 3—Methods for characterization of nanoparticles. In *Advances in Nanomedicine for the Delivery of Therapeutic Nucleic Acids*; Nimesh, S., Chandra, R., Gupta, N., Eds.; Woodhead Publishing: Cambridge, UK, 2017; pp. 43–58.
113. Mdlovu, N.B.; Lin, K.-S.; Weng, M.-T.; Mdlovu, N.V. Formulation and in-vitro evaluations of doxorubicin loaded polymerized magnetic nanocarriers for liver cancer cells. *J. Taiwan Inst. Chem. Eng.* **2021**, *126*, 278–287. [CrossRef]

114. Chapter 16—Gravity Separation. In *Mineral Processing Design and Operations*, 2nd ed.; Gupta, A.; Yan, D. (Eds.) Elsevier: Amsterdam, The Netherlands, 2016; pp. 563–628.
115. Bhattacharjee, S. DLS and zeta potential—What they are and what they are not? *J. Control Release* **2016**, *235*, 337–351. [CrossRef] [PubMed]
116. Ravikumar, C.; Kumar, S.; Bandyopadhyaya, R. Aggregation of dextran coated magnetic nanoparticles in aqueous medium: Experiments and Monte Carlo simulation. *Colloids Surf. A Physicochem. Eng. Asp.* **2012**, *403*, 1–6. [CrossRef]
117. Wu, R.; Liu, J.-H.; Zhao, L.; Zhang, X.; Xie, J.; Yu, B.; Ma, X.; Yang, S.-T.; Wang, H.; Liu, Y. Hydrothermal preparation of magnetic Fe3O4@C nanoparticles for dye adsorption. *J. Environ. Chem. Eng.* **2014**, *2*, 907–913. [CrossRef]
118. Félix, L.L.; Rodriguez Martínez, M.A.; Pacheco Salazar, D.G.; Huamani Coaquira, J.A. One-step synthesis of polyethyleneimine-coated magnetite nanoparticles and their structural, magnetic and power absorption study. *RSC Adv.* **2020**, *10*, 41807–41815. [CrossRef]
119. Suh, J.; Paik, H.J.; Hwang, B.K. Ionization of Poly(ethylenimine) and Poly(allylamine) at Various pH′s. *Bioorganic Chem.* **1994**, *22*, 318–327. [CrossRef]
120. Altalhi, T.A.; Ibrahim, M.M.; Mersal, G.A.M.; Mahmoud, M.H.H.; Kumeria, T.; El-Desouky, M.G.; El-Bindary, A.A.; El-Bindary, M.A. Adsorption of doxorubicin hydrochloride onto thermally treated green adsorbent: Equilibrium, kinetic and thermodynamic studies. *J. Mol. Struct.* **2022**, *1263*, 133160. [CrossRef]
121. Righetti, P.G.; Menozzi, M.; Gianazza, E.; Valentini, L. Protolytic equilibria of doxorubicin as determined by isoelectric focusing and 'electrophoretic titration curves'. *FEBS Lett.* **1979**, *101*, 51–55. [CrossRef]
122. Sturgeon, R.J.; Schulman, S.G. Electronic Absorption Spectra and Protolytic Equilibria of Doxorubicin: Direct Spectrophotometric Determination of Microconstants. *J. Pharm. Sci.* **1977**, *66*, 958–961. [CrossRef]
123. Coluccini, C.; Ng, Y.M.; Reyes, Y.I.A.; Chen, H.-Y.T.; Khung, Y.L. Functionalization of Polyethyleneimine with Hollow Cyclotriveratrylene and Its Subsequent Supramolecular Interaction with Doxorubicin. *Molecules* **2020**, *25*, 5455. [CrossRef]
124. Abasalta, M.; Asefnejad, A.; Khorasani, M.T.; Saadatabadi, A.R.; Irani, M. Adsorption and sustained release of doxorubicin from N-carboxymethyl chitosan/polyvinyl alcohol/poly(ε-caprolactone) composite and core-shell nanofibers. *J. Drug Deliv. Sci. Technol.* **2022**, *67*, 102937. [CrossRef]
125. Wang, Y.; Yang, S.-T.; Wang, Y.; Liu, Y.; Wang, H. Adsorption and desorption of doxorubicin on oxidized carbon nanotubes. *Colloids Surf. B Biointerfaces* **2012**, *97*, 62–69. [CrossRef] [PubMed]
126. Shafiei-Irannejad, V.; Rahimkhoei, V.; Molaparast, M.; Akbari, A. Synthesis and characterization of novel hybrid nanomaterials based on β-cyclodextrine grafted halloysite nanotubes for delivery of doxorubicin to MCF-7 cell line. *J. Mol. Struct.* **2022**, *1262*, 133004. [CrossRef]
127. Mdlovu, N.V.; Lin, K.-S.; Weng, M.-T.; Hsieh, C.-C.; Lin, Y.-S.; Carrera Espinoza, M.J. In vitro intracellular studies of pH and thermo-triggered doxorubicin conjugated magnetic SBA-15 mesoporous nanocarriers for anticancer activity against hepatocellular carcinoma. *J. Ind. Eng. Chem.* **2021**, *102*, 1–16. [CrossRef]
128. Jiang, X.; Zhang, D.; Sun, R.; Wang, H.; Yang, Y.; Guo, H.; Tang, Y. A combined experimental and molecular dynamics simulation study on doxorubicin adsorption on strontium-substituted hydroxyapatite hollow microspheres. *Appl. Surf. Sci.* **2021**, *542*, 148667. [CrossRef]
129. Akturk, O. The anticancer activity of doxorubicin-loaded levan-functionalized gold nanoparticles synthesized by laser ablation. *Int. J. Biol. Macromol.* **2022**, *196*, 72–85. [CrossRef]
130. Sezer, A.D.; Kazak Sarılmışer, H.; Rayaman, E.; Çevikbaş, A.; Öner, E.T.; Akbuğa, J. Development and characterization of vancomycin-loaded levan-based microparticular system for drug delivery. *Pharm. Dev. Technol.* **2017**, *22*, 627–634. [CrossRef]
131. García, L.; Garaio, E.; López-Ortega, A.; Galarreta-Rodriguez, I.; Cervera-Gabalda, L.; Cruz-Quesada, G.; Cornejo, A.; Garrido, J.J.; Gómez-Polo, C.; Pérez-Landazábal, J.I. $Fe_3O_4$–$SiO_2$ Mesoporous Core/Shell Nanoparticles for Magnetic Field-Induced Ibuprofen-Controlled Release. *Langmuir* **2022**, *39*, 211–219. [CrossRef]
132. Polystyrene sulfonates. In *Meyler's Side Effects of Drugs*, 6th ed.; Aronson, J.K. (Ed.) Elsevier: Oxford, UK, 2016; pp. 868–871.
133. Herold, B.C.; Bourne, N.; Marcellino, D.; Kirkpatrick, R.; Mosoian, A.; Klotman, M.; Strauss, D.; Anderson, R.; Zanenveld, L.; Cooper, M.; et al. Polystyrene Sulfonate Is a Safe and Effective Candidate Topical Antimicrobial for the Prevention of Sexually Transmitted Diseases. *Pediatr. Res.* **1999**, *45*, 163. [CrossRef]
134. Naumov, A.A.; Dubrovskii, A.V.; Musin, E.V.; Kim, A.L.; Potselueva, M.M.; Tikhonenko, S.A. A Study of the Cytotoxic Effect of Microcapsules and Their Constituent Polymers on Macrophages and Tumor Cells. *Bull. Exp. Biol. Med.* **2018**, *166*, 69–74. [CrossRef]
135. Kafil, V.; Omidi, Y. Cytotoxic impacts of linear and branched polyethylenimine nanostructures in a431 cells. *BioImpacts BI* **2011**, *1*, 23–30. [CrossRef]
136. Brunot, C.; Ponsonnet, L.; Lagneau, C.; Farge, P.; Picart, C.; Grosgogeat, B. Cytotoxicity of polyethyleneimine (PEI), precursor base layer of polyelectrolyte multilayer films. *Biomaterials* **2007**, *28*, 632–640. [CrossRef] [PubMed]
137. Moghimi, S.M.; Symonds, P.; Murray, J.C.; Hunter, A.C.; Debska, G.; Szewczyk, A. A two-stage poly(ethylenimine)-mediated cytotoxicity: Implications for gene transfer/therapy. *Mol. Ther. J. Am. Soc. Gene Ther.* **2005**, *11*, 990–995. [CrossRef] [PubMed]
138. Morimoto, K.; Nishikawa, M.; Kawakami, S.; Nakano, T.; Hattori, Y.; Fumoto, S.; Yamashita, F.; Hashida, M. Molecular weight-dependent gene transfection activity of unmodified and galactosylated polyethyleneimine on hepatoma cells and mouse liver. *Mol. Ther. J. Am. Soc. Gene Ther.* **2003**, *7*, 254–261. [CrossRef] [PubMed]

139. Dragar, Č.; Kralj, S.; Kocbek, P. Bioevaluation methods for iron-oxide-based magnetic nanoparticles. *Int. J. Pharm.* **2021**, *597*, 120348. [CrossRef]
140. Ghazanfari, M.R.; Kashefi, M.; Shams, S.F.; Jaafari, M.R. Perspective of $Fe_3O_4$ Nanoparticles Role in Biomedical Applications. *Biochem. Res. Int.* **2016**, *2016*, 7840161. [CrossRef] [PubMed]
141. Stamopoulos, D.; Manios, E.; Gogola, V.; Niarchos, D.; Pissas, M. On the biocompatibility of $Fe_3O_4$ ferromagnetic nanoparticles with human blood cells. *J. Nanosci. Nanotechnol.* **2010**, *10*, 6110–6115. [CrossRef]
142. Khabibullin, V.R.; Stepanov, G.V. Effect of a Low-Frequency Magnetic Field on the Release of Heat by Magnetic Nanoparticles of Different Shapes. *Russ. J. Phys. Chem. A* **2020**, *94*, 439–444. [CrossRef]
143. Egunova, O.R.; Reshetnikova, I.S.; Kazimirova, K.O.; Shtykov, S.N. Magnetic Solid-Phase Extraction and Fluorimetric Determination of Some Fluoroquinolones. *J. Anal. Chem.* **2020**, *75*, 24–33. [CrossRef]
144. Huang, H.J.; Chetyrkina, M.; Wong, C.W.; Kraevaya, O.A.; Zhilenkov, A.V.; Voronov, II; Wang, P.H.; Troshin, P.A.; Hsu, S.H. Identification of potential descriptors of water-soluble fullerene derivatives responsible for antitumor effects on lung cancer cells via QSAR analysis. *Comput. Struct. Biotechnol. J.* **2021**, *19*, 812–825. [CrossRef]
145. Nechipurenko, D.Y.; Receveur, N.; Yakimenko, A.O.; Shepelyuk, T.O.; Yakusheva, A.A.; Kerimov, R.R.; Obydennyy, S.I.; Eckly, A.; Léon, C.; Gachet, C.; et al. Clot Contraction Drives the Translocation of Procoagulant Platelets to Thrombus Surface. *Arterioscler. Thromb. Vasc. Biol.* **2019**, *39*, 37–47. [CrossRef] [PubMed]